ACS OMEGA

Open Access

http://pubs.acs.org/journal/acsodf

Article

Structure-Based Discovery of Allosteric Inhibitors Targeting a New Druggable Site in the Respiratory Syncytial Virus Polymerase

Ahmed K. Oraby, Leanne Bilawchuk, Frederick G. West,* and David J. Marchant*

Cite This: *ACS Omega* 2024, 9, 22213−22229

Read Online

ACCESS | Metrics & More | Article Recommendations | Supporting Information

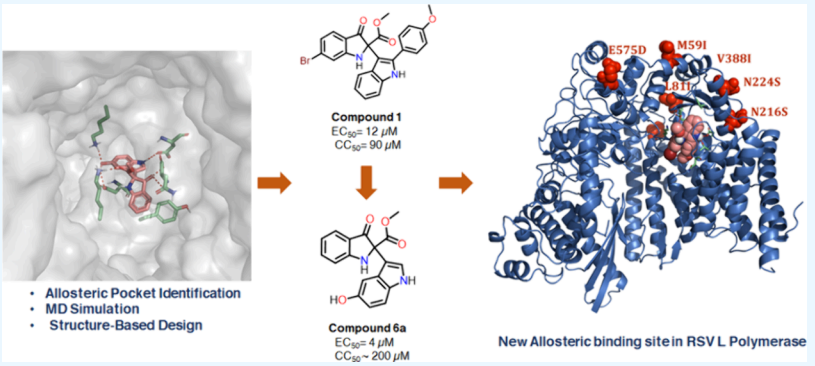

ABSTRACT: Respiratory syncytial virus (RSV) is a major cause of severe lower respiratory infections for which effective treatment options remain limited. Herein, we employed a computational structure-based design strategy aimed at identifying potential targets for a new class of allosteric inhibitors. Our investigation led to the discovery of a previously undisclosed allosteric binding site within the RSV polymerase, the large (L) protein. This discovery was achieved through a combination of virtual screening and molecular dynamics simulations. Subsequently, we identified two inhibitors, **6a** and **10b**, which both exhibited promising antiviral activity in the low micromolar range. Resistance profiling revealed a distinctive pattern in how RSV evaded treatment with this class of inhibitors. This pattern strongly suggested that this class of small molecules was targeting a new binding site in the RSV L protein, aligning with the computational predictions made in our study. This study paves the way for the development of more potent inhibitors for combating RSV infections by targeting a new druggable pocket within the RdRp which does not overlap with previously known resistance sites.

INTRODUCTION

Human respiratory syncytial virus (RSV) is the leading cause of upper and lower respiratory tract infections in pediatric patients worldwide. The severity of RSV infections is greatest in infants and immunocompromised adults with approximately 60,000 children under the age of 5 and ∼ 177,000 adults hospitalized in the USA yearly.[1−4] The viral infection can progress from the upper to the lower respiratory tract which can result in more complicated symptoms and illness including pneumonia, bronchiolitis, asthma, and, in some cases, cardiopulmonary distress.[5−7]

Although the virus was first isolated in 1955 from chimpanzees, only recently was a vaccine approved for the prevention of RSV-related respiratory infections in adults.[8] However, in pediatrics, there are limited drug treatment options beyond the prophylactic drug palivizumab, an expensive monoclonal antibody (mAB) used only for high-risk premature infants.[9,10] Recently, a single injection of Nirsevimab, a monoclonal antibody that targets the RSV fusion protein, has proven to protect infants from RSV associated lower respiratory tract infection.[11] Ribavirin, a well-known antiviral drug, was approved for aerosol treatment against RSV infections; however, its use has been curtailed due to risks of carcinogenic and teratogenic effects.[12] In summary, the absence of any effective small-molecule antiviral drugs represents a significant unmet need in the healthcare delivery system.

RSV exists as two subtypes, A and B, which are found within the genus *Orthopneumovirus*, family *Pneumoviridae*, order *Mononegavirales*. RSV is an enveloped, negative-sense, single-stranded (ss) RNA virus with spherical virion particles of 100−350 nm in diameter or long filaments of 60−200 nm in diameter.[13] The RSV genome is 15.2 kb and codes for 11 proteins: nonstructural proteins (NS-1 and NS-2), matrix

Received: February 6, 2024
Revised: April 8, 2024
Accepted: April 12, 2024
Published: May 6, 2024

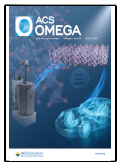

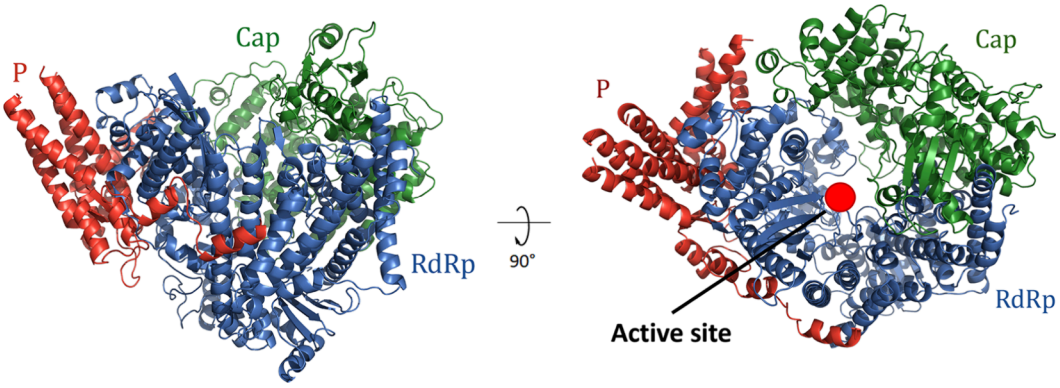

Figure 1. RSV L protein domains (domains are color-coded). The P protein tetramer is shown in red color, the RdRp domain in blue, and the capping domain in green (PDB ID 6PZK). The figure was generated using PyMOL.[23] Reproduced with permission from ref 20. Copyright 2024 Elsevier.

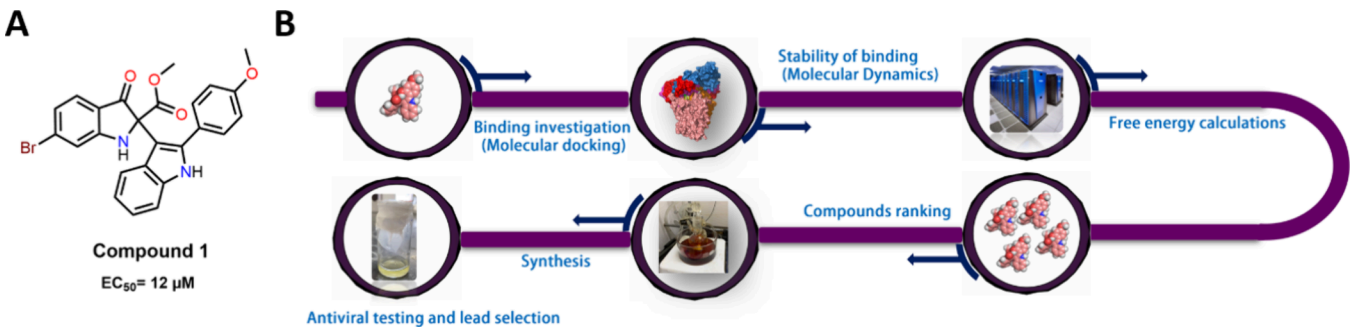

Figure 2. (A) Structure of compound **1**. (B) Flowchart of the virtual screening and computational investigations performed in this work.

protein (M), nucleoprotein (N), phosphoprotein (P), polymerase (L), small hydrophobic protein (SH), glycoprotein (G), fusion protein (F), M2-1 and M2-2proteins.[14,15]

Several targets have been investigated for the development of an effective therapeutic agent against RSV infections. Viral RNA and DNA polymerases are among the most attractive targets for inhibition of viral replication and targeting these proteins is the most common approach for antiviral drug development due to its critical role in regulating viral replication.[16] RSV contains a nonsegmented negative-sense RNA genome, which requires the virus-encoded RNA-dependent RNA polymerase (RdRp) complex for genome replication and transcription of viral RNA.[17] Three viral proteins are essential for the replication of the RSV genome: the nucleoprotein (N), the large protein (L), and the phosphoprotein (P). The large polymerase protein (L) contains the enzymatic domains involved in the transcription and replication, and the phosphoprotein (P) acts as an essential cofactor (Figure 1).[18−20] Recent approaches in drug development have identified several chemical moieties that can effectively inhibit RSV replication complexes.[21] However, the continuous search for small molecules with high potency, selectivity, and improved pharmacokinetics remains an ongoing field.

Our group previously reported a series of bis-indole compounds inspired by the natural product isatisine A with demonstrated antiviral activity against RSV and Zika viruses.[22] In the present study, we have carried out a structure-based drug discovery campaign to identify the exact target of previously discovered RSV anti-infective agents for which the replication complex had been identified as the likely target. Molecular docking and molecular dynamics (MD) simulations were carried out to evaluate the possible binding pocket and mode of the previously reported polymerase inhibitors and correlate the activity observed with the computational results (Figure 2). These approaches could lead to a better understanding of the mechanism by which these molecules inhibit viral replication with the ultimate goal of designing more potent inhibitors.

RESULTS AND DISCUSSION

Assessment of The Replication Complex for Putative Druggable Pockets. Our previous findings support that this class of bis-indole compounds is targeting the replication complex of RSV,[22] which consists of the RSV viral RNA-dependent RNA polymerase large (L) protein and phosphoprotein (P). In this work, we chose to narrow down our search approach and focus on the L protein as the primary target. In this context, computational docking and MD simulations were employed to elucidate any potential binding with RSV L protein.

The 250 kDa L protein harbors three conserved enzymatic domains: the RNA-dependent RNA polymerase (RdRp) domain, the polyribonucleotidyl-transferase (PRNTase or capping domain), and the methyltransferase (MTase) domain (Figure 1).[24] The cryo-EM structure of wild-type RSV L protein was experimentally reported in 2019 which facilitated our computational investigations.[20]

Initially, the fpocket script, Site Finder implemented in MOE, and SiteMap utility implemented in the Schrodinger discovery suite were used to identify putative RSV L binding pockets.[25−28] This approach identified 122 possible pockets within the Cryo-EM structure of the L protein with a

https://doi.org/10.1021/acsomega.4c01207
ACS Omega 2024, 9, 22213−22229

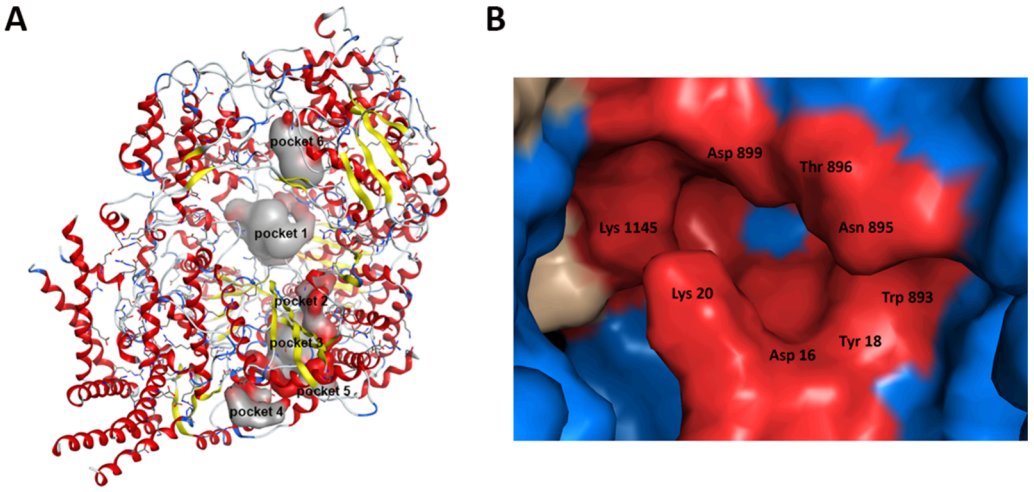

Figure 3. Allosteric Pocket on the RSV L protein in complex with the P protein. (A) Druggable pockets identified in the L protein. (B) Surface representation of pocket 1 highlighting key pocket residues in red.

druggability score ranging from 0 to 0.99 on a scoring range between 0 and 1, where a score of 1 would indicate a theoretically ideal druggable site. The search was narrowed down by ranking pockets using druggability scores and comparing pockets identified by each program, which downsized the search to six possible druggable pockets, including the active site (Figure 3). Among the examined pockets, pocket 1 is located in close proximity to the template and NTP entry channels and is formed of charged amino acids, which aid in the placement of incoming NTPs to be placed in the active site.[20,29,30] The pocket had a druggability score of 0.99, and a volume of ∼490 Å^3, and the electrostatic aspects were taken into consideration in supporting the selection of this pocket. Visual inspection of the Cryo-EM structure of L protein revealed that the pocket is surrounded by several positively charged residues including R621, R747, K20, and K540, which line the NTP entry tunnel (Figure S1). These observations could support the possibility that binding of non-nucleoside inhibitors to this pocket could interfere with the incoming NTPs, the placement of the template in the active site, or by allosterically altering the conformation of the active site, which will subsequently inhibit viral replication.

Molecular Dynamics Simulations of the *Apo* RSV L-P Complex. Molecular dynamics has been used widely in validating and refining docking poses to shed light on an accurate representation of ligand−protein interactions.[31] Initially, missing loop residues (609−626) from the cryo-EM map were built and refined using the Prime module implemented in Schrödinger Suite.[32] To understand the dynamicity of the RSV L-P complex in the unbound state, a 100 ns long MD simulation of the *apo* structure (PDB ID: 6PZK) was performed. The RMSD of the protein backbone equilibrated around 15 ns, and once a stable conformation was achieved, the system remained stable with a fluctuation of 1.7 Å from its initial coordinates over the whole simulation (Figure S2). The flexibility of residues was further analyzed using the atomic fluctuation (beta factors) of the protein backbone atoms. The majority of the residues were stable during the whole simulation with the most flexible regions occurring at the N and C termini of the protein. In addition, a region from residues 220−250 displayed elasticity during our MD trajectories. Despite the displayed flexibility within this region, the RSV L-P complex appeared to be quite stable. To evaluate the potential accessibility of this pocket to small molecules, the water hydration was studied by counting the number of water molecules within the first and second hydration shells throughout the MD simulation. The selected pocket allowed up to 30 water molecules to enter in the first hydration shell while allowing 105 to 120 water molecules in the second hydration shell (Figure S2). Moreover, the pocket volume was reassessed throughout the MD trajectories using MDpocket.[33] MDpocket analysis revealed that this pocket has an average volume of around ∼517 Å^3, enough to accommodate a small molecule (Figure S3). These results support the possibility that this site could be targeted with small molecules. Clusters from the whole simulation trajectory were generated, and the lowest energy cluster was then used for docking purposes. Interestingly, the pocket is located away from the residues that form the QUAD mutations responsible for viral escape arising from nucleoside analog inhibitors such as ALS-8112.[34] Moreover, sequence alignment of other negative-stranded viruses that have a similar RdRp structure revealed that the residues in pocket 1 are conserved among the Mononegavirales viruses analyzed (Figure S4). It is worth mentioning that Kleiner et al.[35] recently described the cryo-EM structure of an allosteric inhibitor (MRK-1) in complex with the RSV and human metapneumovirus (HMPV) polymerases that do not overlap with the binding site described herein nor do any previously described allosteric inhibitor such as AZ-27 or YM-53403, to which RSV quickly developed resistance.[36] We believe that if targeting this pocket is successful, it could potentially identify a new class of inhibitors with a novel mechanism of viral protein inhibition.

Putative Binding Poses of The New Bis-Indole Compounds. Our previously reported hit, compound **1**, was used as a docking control since it had shown the best antiviral activity against RSV.[22] Compound **1** inhibited RSV-induced cytopathic effect with an EC_{50} of 12 μM. To explore how the compounds could potentially bind in the identified pockets, molecular docking was employed, and the binding pose and docking score were evaluated. Examination of the binding poses of **1** and the correlation between docking scores and the antiviral activity revealed that the compound could possibly be binding to pocket 1 with a docking score of −6.4 kcal/mol, as calculated using the the Extra Precision (XP) Glide scoring function implemented in Schrödinger Suite.[37] Analysis of the

https://doi.org/10.1021/acsomega.4c01207
ACS Omega 2024, 9, 22213−22229

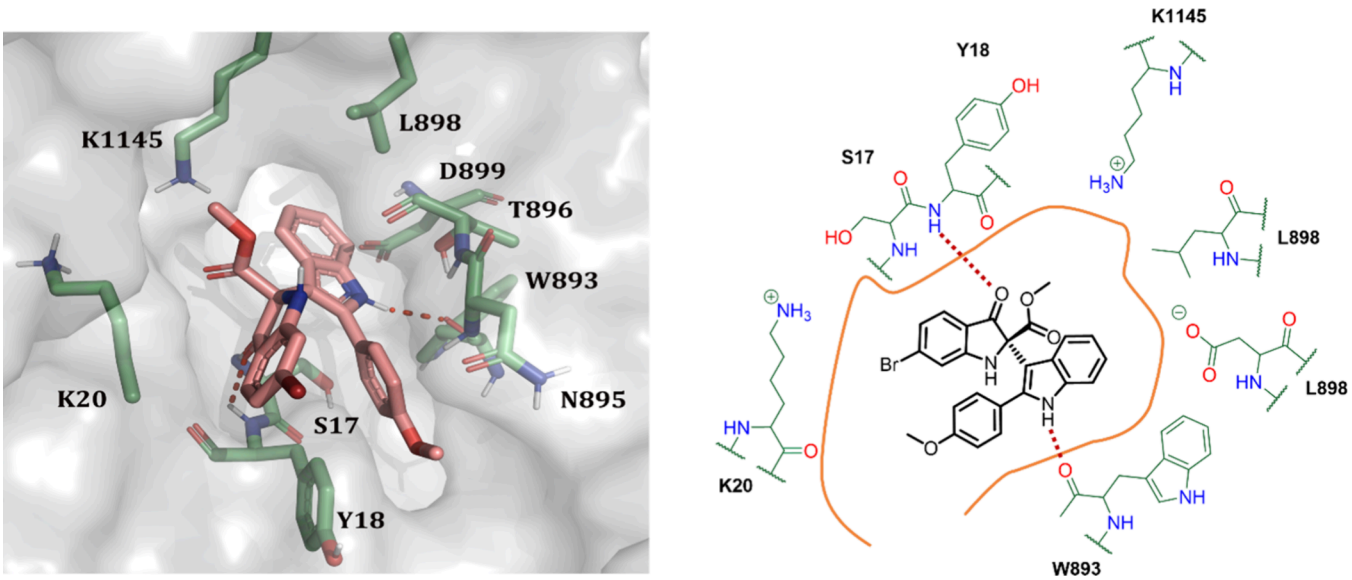

Figure 4. Putative docking pose of compound **1** (left) and 2D representation of the ligand−protein interactions (right). Predicted hydrogen bonds are shown as red dotted lines.

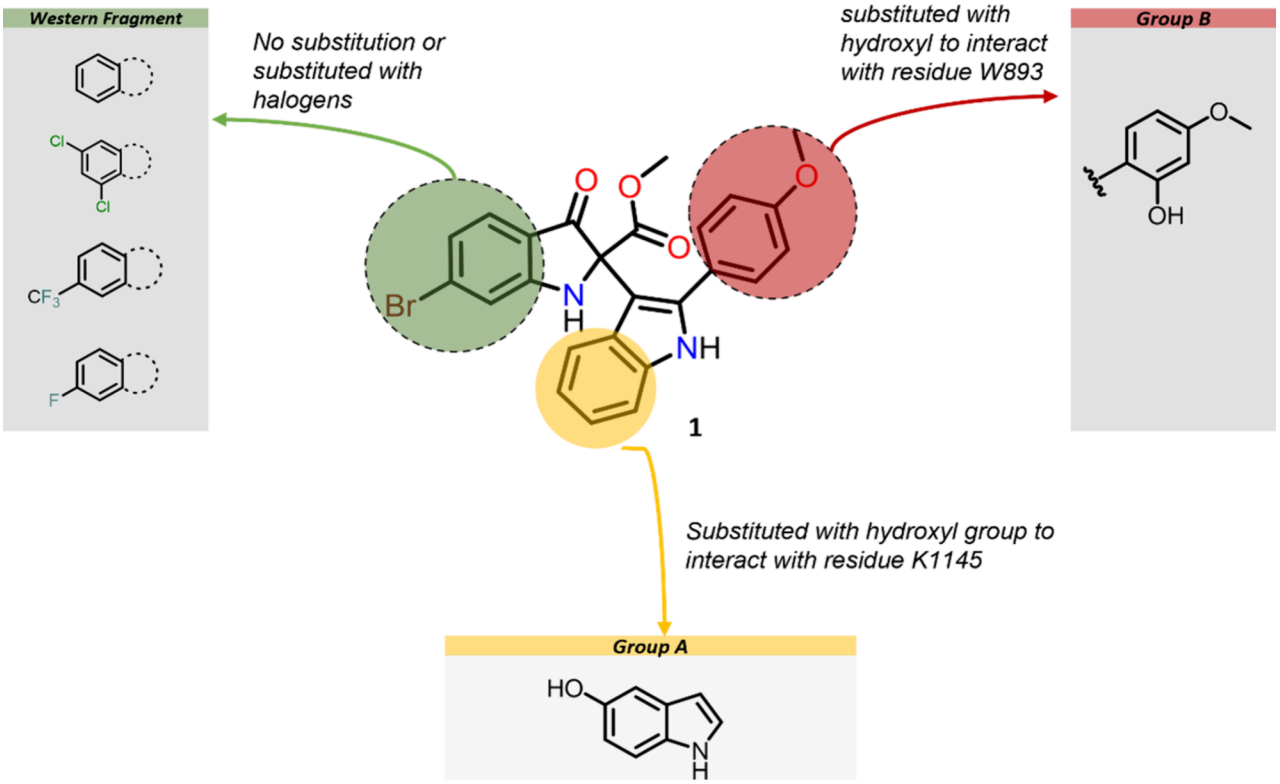

Figure 5. Summary of new derivatives design for SAR investigation as RSV RdRp inhibitors.

ligand−protein complex revealed that the compound formed two hydrogen bonds with residues S17 and W893 (Figure 4). Although the active site of the L protein is usually considered to be the primary target of any docking simulations, it has been excluded from our search due to apparent structural differences between nucleoside inhibitors and this class of compounds. This assumption was further confirmed by docking of compound **1** in the active site, which showed a negligible docking score of −3.2 kcal/mol.

Design of the New Analogues. Given the ligand−protein interactions observed for compound **1** in the putative binding pose with the RSV L, we asked whether modifying the indole part of the parent compound could be beneficial and could lead to enhanced ligand−protein interactions. Visual inspection of the binding pocket revealed that several residues could contribute to better binding of the lead compound with the L protein. In this regard, we wanted to build a stronger hydrogen bonding network to increase the capacity of the ligand−protein binding and stability following a detailed

https://doi.org/10.1021/acsomega.4c01207
ACS Omega 2024, 9, 22213−22229

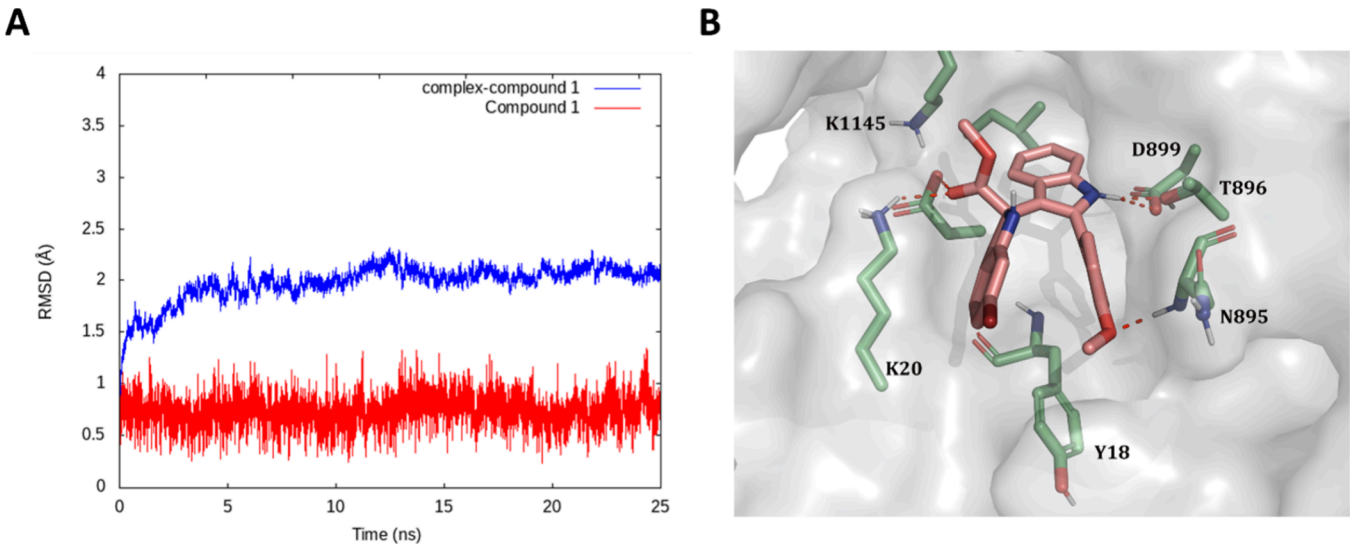

Figure 6. MD analysis of compound **1**. (A) RMSD trends of compound **1** in complex with the L protein. (B) MD snapshot suggesting the putative binding pose of compound **1**.

computational analysis of the hydrophobic and hydrophilic properties in the selected pocket. Initial consideration was given to substitution with a hydroxyl group on the C5 of the indole as this may result in a new hydrogen bond contact with residue K1145 (Figure 5). Moreover, the removal of the aryl moiety at the indole C2 position was also considered as a means to evaluate the minimum requirements for the activity of this class of inhibitors. These modifications were divided into two groups of compounds where group A would have the aryl substitution at the C2 of the indole removed and an additional hydroxyl group would be added at the C5 of the indole and group B will have a single modification on 2-phenylindole moiety (Figure S5).

A newly designed library of compounds was used for the initial virtual screening. Docking simulations of Group A showed that the absence of the 2-aryl substitution on the indole moiety could be tolerated. Compound **6a** exhibited five hydrogen bond interactions to residues (N895, D899, D16, K20, and K1145) with a docking score of −7.21 kcal/mol. Virtual screening of this library was performed, and the best scoring poses for each analog was retained for further investigation using MD simulations. Since compound **1** and its analogs are racemic, evaluation of each enantiomer was crucial to determine which isomer would be more suitable for binding and complementing the pocket cavity. Initially, both enantiomers were docked, and the higher scoring enantiomer was carried forward for the molecular dynamics simulation (MD). The (*S*) enantiomer exhibited better binding poses for most of the newly designed compounds, with docking scores ≥6 kcal/mol and hence was selected for MD simulations.

Assessment of Ligands Stability and Poses During MD Simulation. To evaluate the stability of the L protein complex during MD simulations, the root-mean-square deviation (RMSD) value was calculated over a 25 ns long simulation time. Analysis of the trajectories indicated that the *S* isomer of compound **1** was more stable in the binding site during the simulation with an average RMSD for the complex of 2.1 Å. The compound showed very strong stability in the complex with a small deviation of 0.74 Å from the original coordinates throughout the whole trajectory (Figure 6). A representative structure of the last 15 ns of simulation for all ligands was obtained using clustering in AMBER tools via the average-linkage algorithm. Based on the stability observed for the protein−ligand complexes, we set the simulation time to 25 ns to evaluate all complexes. Analysis of the trajectories revealed that the carbonyl oxygen of the ester forms a hydrogen bond with the positively charged ε-amino group of residue K20. The nitrogen of the 4-methoxyphenyl indole part of the molecule interacted extensively with side chains of residues D899 and T896 through hydrogen bonding. Moreover, the methoxy oxygen formed a hydrogen bond with the backbone of residue N895. The ligand orientation placed the benzene part of the indole skeleton into a hydrophobic pocket formed of residues L14, I896, and L898, which contributed to a more efficient binding by filling the pocket (Figure 6).

The results of compound **1** stability motivated us to explore the tolerability of different functionalities on this moiety. Interestingly, the absence of the 2-phenyl substitution on the indole did not affect the stability of the ligand binding and the whole complex for a simulation of 50 ns.

Importantly, the extended simulation time was crucial at this stage to further validate the results and to avoid any false positives. The binding of compound **6a** to the RSV L protein stabilized the replication complex with a mean RMSD of 1.8 Å and a ligand RMSD of 0.65 Å (Figure 7). The orientation of **6a** was similar to that of compound **1** in the binding pocket with a small deviation in which the 5-hydroxyl group was placed near residue K1145. This orientation led to the desired hydrogen bond interaction between the phenolic oxygen of the molecule and the hydrogen of the lysine side chain. Interestingly, the compound occupied a hydrophobic cleft inside the pocket and the substitutions complemented the electrostatic interactions required for that pocket as shown in (Figure 7). These results suggested that modifications of the bis-indole parent molecule could be tolerable and might lead to a more potent inhibitor.

Based on the previous results, another generation of compounds based on **6a** was investigated. In this generation, group B, the core structure of the parent compound **1**, was maintained. The presence of a methoxy group at the C4 was believed to decrease the cytotoxicity of this class of compounds.[22] In this work, the introduction of a hydroxyl group at C2 of the 2-phenyl-4-methoxyindole is sought to

https://doi.org/10.1021/acsomega.4c01207
ACS Omega 2024, 9, 22213−22229

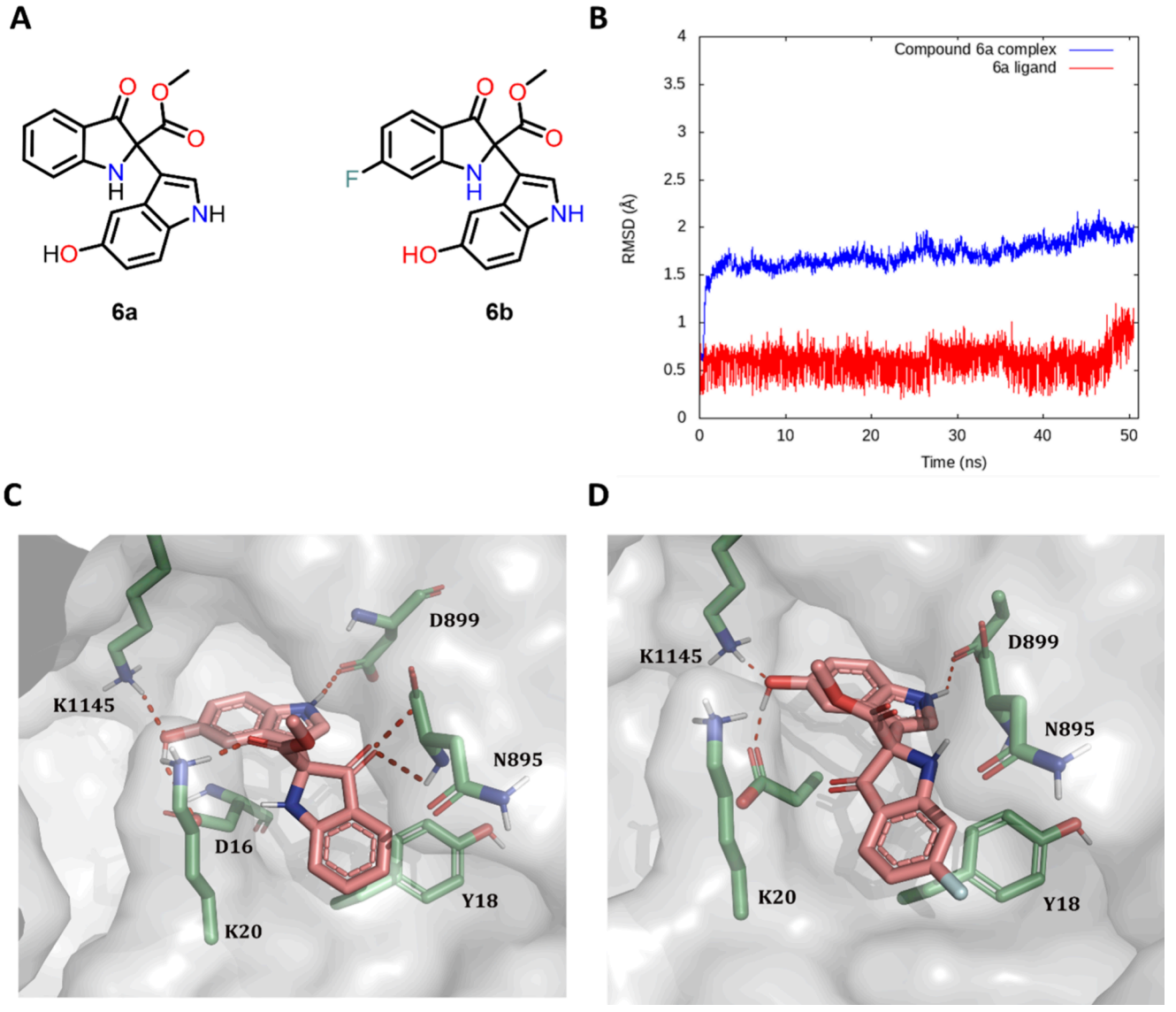

Figure 7. Binding poses of Group A compounds. (A) Chemical structures of compounds **6a** and **6b** from Group A. (B) RMSD of the backbone atoms of compound **6a** in complex with L protein. (C) MD snapshot of compound **6a** binding pose. (D) MD snapshot of compound **6b** binding pose (hydrogen bonds are shown as red dashed lines).

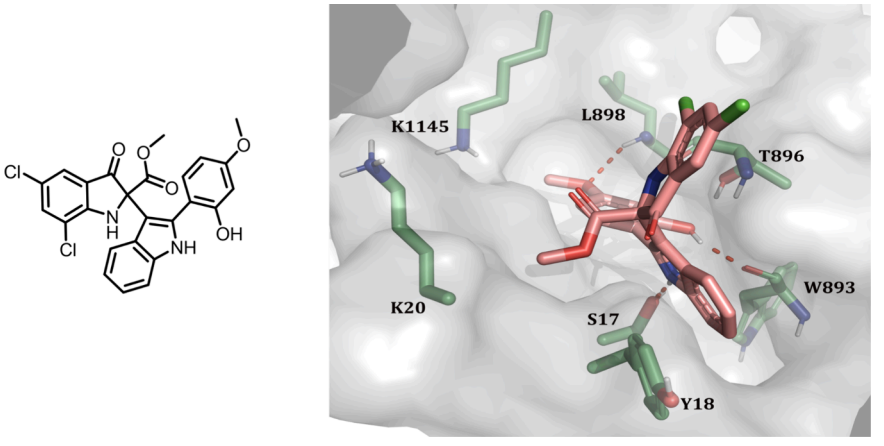

Figure 8. Chemical Structure of compound **10b** (left) and the lowest energy MD snapshot of the ligand−protein complex (right). Hydrogen bonds are depicted as red dashed lines.

https://doi.org/10.1021/acsomega.4c01207
ACS Omega 2024, 9, 22213−22229

Scheme 1. Synthesis of Group A Compounds[a]

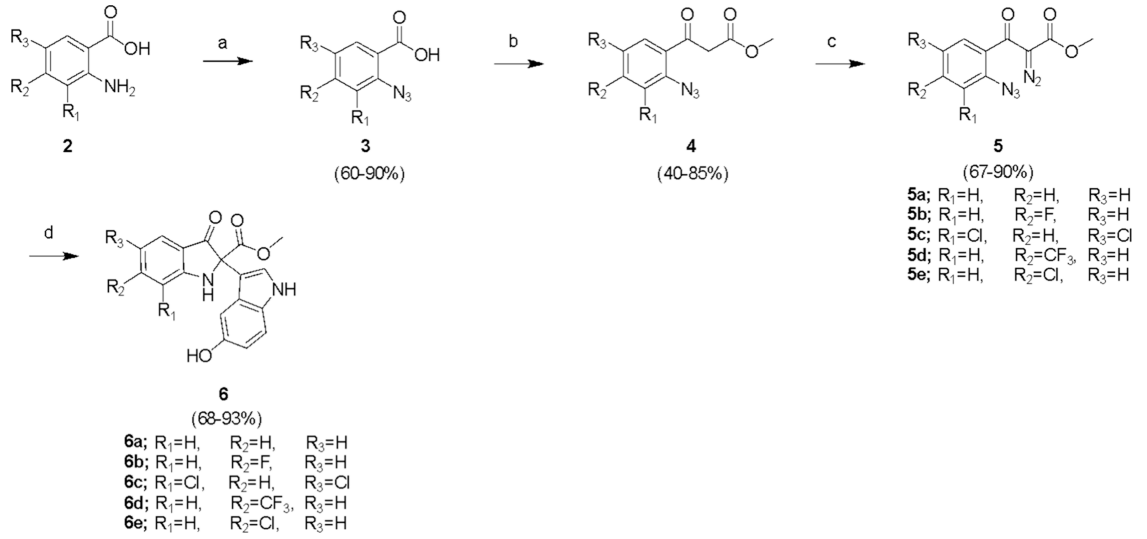

[a]Reagents and conditions: (a) $NaNO_2$, aq. HCl, NaN_3, H_2O, 0 °C; (b) (i) trichloroacetyl chloride, methyl acetate, NaH, DCM, 0 °C (ii) *N*-methylimidazole, −45 °C, (iii) $TiCl_4$, Et_3N, −45 °C; (c) TsN_3, Et_3N, CH_3CN, rt; (d) 10 mol % $Cu(OTf)_2$, 5-hydroxyindole, DCM, rt.

potentially contribute to an enhanced hydrogen bond network within the pocket. In contrast to previously observed binding modes, the indole part of compounds **10b−e** flipped from its initial position, after 10 ns of the simulation, forcing the ligands to rotate inside the pocket, perhaps to avoid solvent exposure (Figure 8). Although this rotation did not result in any hydrogen bond contact with K1145, the ligands were still able to build more hydrogen bonds within the pocket. Ligands maintained some of the previously observed hydrogen bonds to D16, T896, and N895. An additional hydrogen bond was established between the C2 (−OH) and the backbone oxygen of W893 as demonstrated in the putative binding of compound **10b** (Figure 8). Although the results were very compelling, an accurate binding free energy calculation was needed to rank the compounds and understand the ligand contributions to the binding.

Relative Binding Free Energy Analysis of Ligand−Protein Complexes. The combination of MD simulations and end-point free energy calculation such as the molecular mechanics/generalized Born surface area (MM/GBSA) has proven to be very useful in the accurate assessment of protein−ligand complexes.[38−40] Building on our previous analysis, the MM-GBSA method was employed on the snapshots of the complexes sampled from the MD trajectories to get better insights into ligand contributions to binding. The trajectory of each complex was sampled at an interval of 10 ps from the last 10 ns of the simulation to yield 100 frames for the MM-GBSA rescoring.

Compounds **6c**, **6e**, **10c**, and **10e** showed weak binding affinities to the RSV L with values of −24.31 ± 3.6, −24.84 ± 2.6, −22.11 ± 4.6, and −22.25 ± 4.7 kcal/mol, respectively (Table S1). Further, per-residue decomposition analysis was performed to obtain the energetic contributions of each residue in the binding pocket toward inhibitor binding. The residues that consistently contributed to the binding of compound **1** were identified as D16, S17, Y18, T896, and I897, where van der Waals interactions dominated the binding. Moreover, the analysis indicated that D899 contributed mainly to electrostatic interactions as summarized in Table S2. However, energy decomposition for compound **6a** revealed that most pocket residues contributed a small portion to van der Waals interactions while electrostatic interactions by D899 and T896 were more dominant as shown in Table S2. Based on these results, the two computationally investigated libraries were synthesized and evaluated for their antiviral activities to build a more accurate SAR based on their antiviral activity.

Chemical Synthesis. To explore the structure−activity relationships (SAR) at the western part of the bis-indole scaffold, the synthesis of several analogues of Group A was achieved according to the route outlined in Scheme 1 and according to a previously published literature procedure.[22]

Starting from commercially available anthranilic acid derivatives, the route began with a diazotization reaction followed by the addition of sodium azide to afford compound **3**. The beta-keto ester compound **4** was formed, according to the Ti-crossed-Claisen condensation reported by Misaki et al.,[41] from the reaction of the carboxylic acid **2** with trichloroacetyl chloride and methyl acetate promoted by $TiCl_4$ and *N*-methylimidazole at −45 °C to furnish this intermediate in good yields. The Regitz-diazo transfer was the key step to produce the diazo-azide intermediate **5** by the reaction of **4** with tosyl azide in the presence of triethylamine at room temperature for 12 h.

The synthesis of targeted bis(indole) compounds processed through a dual catalytic cycle described previously by our group.[22] In this dual catalytic cycle, intermediate **5** was treated with 10 mol % of $Cu(OTf)_2$ in DCM to catalytically produce copper metallocarbenes after an *in situ* reduction of copper(II) precatalyst to copper(I) by the indole as the reducing agent. This led to the conversion of **5** into a *C*-acylimine intermediate followed by Brønsted acid activation of the imine for the Fridel-Crafts alkylation of the indole trap. This step produced our targeted compounds **6a−e** in good to moderate yields. In order to prepare targeted compounds **10a−e**, the intermediate 2-(1*H*-indol-2-yl)-5-methoxy phenol **9** was synthesized through Fischer indole synthesis by reacting 2′-hydroxy-4′-methoxyacetophenone **7** with phenyl hydrazine under acidic conditions which gave the desired product in 68% yield as shown in Scheme 2.[42] The synthesis of compounds **10a−e** followed the synthetic route discussed above but using

https://doi.org/10.1021/acsomega.4c01207
ACS Omega 2024, 9, 22213−22229

compound **9** instead of 5-hydroxy indole as shown in Scheme 3.

Scheme 2. Synthesis of Intermediate Compound 9[a]

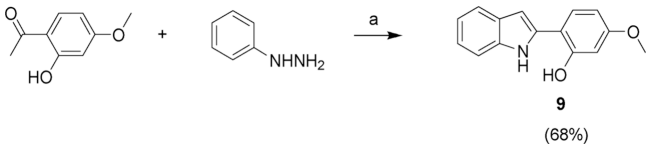

[a]Reagents and conditions: (i) glacial acetic acid, EtOH, reflux. (ii) Polyphosphoric acid, 120 °C.

Evaluation of the Antiviral Activity of the Designed Bis-indole Compounds against RSV. To investigate the antiviral activity of the newly designed compounds against RSV, all compounds from both groups were evaluated to establish a more extensive SAR and to validate our model. The antiviral activity of the bis-indole compounds was evaluated by the cell-based virus replication assay, measuring RSV viral progeny inhibition as a measure of antiviral efficacy. A 10 μM concentration of the compounds was the threshold for determining antiviral activity. Among the tested compounds from group A, compound **6a** showed significant reduction in RSV progeny production in the progeny inhibition assay with an EC_{50} = 4 μM in the RSV-GFP reporter assay (Figure 9A,B). The compound had no effect on the cell viability at test concentrations ($CC_{50} \approx 200$ μM) with a selectivity index (SI = 50). Although compounds **6b** and **6c** share the same scaffold but with different substituents on the indolinone fragment, both compounds exhibited a nonsignificant reduction of the RSV progeny production compared to **6a**, which has no substitutions on the indolinone part. Antiviral evaluation of group B compounds revealed that compound **10b** (which has two chlorines at R_1 and R_3 on the indolinone fragment) is the only compound with significant antiviral activity with an EC_{50} of 6.32 μM (Figure 9C,D).

These results confirm the antiviral activity observed in the viral progeny assay and come in agreement with our computational model where compounds **6a** and **10b** showed a relative binding free energy of −37.60 ± 2.7 and −35.47 ± 2.1 kcal/mol and complemented the conformation of the allosteric binding site while the rest of the tested compounds exhibited a relatively low binding free energy ranging from −22.11 to −34.55 kcal/mol. Based on these precedents, it is notable that the substitutions on the bis-indole significantly affect their antiviral activity.

Resistance Profile of the Bis-indole Chemotype. The emergence of viral resistance following treatment with antiviral drugs provides a challenge for future use of the drug, especially if mutants arise quickly and/or are then transmitted to become dominant circulating variants. Experimental elucidation of susceptibility to resistance is therefore important to identify potential for generation of viral resistance but also identifying the drug mechanism of action. Our previous efforts to develop a resistant mutant against the lead compound **1** were unsuccessful even with 14 serial passages over 5 weeks.[22] This may suggest that there is a high barrier to development of resistant mutations to evade this class of compounds.

To gain insights into the binding site of this class of compounds, a viral evolution assay was explored where the virus was serially passaged in the presence of two concentrations (10 and 25 μM) of compound **1** for 20 passages to force the virus to evade the treatment and develop resistance. At passage 6, we first noted the appearance of mutations in the RSV-L gene that were associated with rebound viral titer in their respective biological replicate (Figure S6). We noted that these mutations were represented by 100% of the quasispecies by passage number 20 when the titer started to rebound. Genome sequencing revealed unique substitutions that affected residues within the RdRp domains, namely, M59I, L81I, N216S, N224S, and V338I. All mutations were located in close proximity and clustered near the computationally identified bis-indole binding site (Figure 10).

These resistance sites are unique and were not associated with escape from previously reported RSV allosteric polymerase inhibitors. Moreover, the sites of these resistant mutants were not located near the P binding sites, suggesting that these compounds do not interfere with P binding to the L protein for polymerase processivity.

Based on our sequence alignment with other negative-stranded RNA viruses (Figure S4), the mutated residues were not conserved whereas the binding site residues were conserved and were likely not able to be mutated and maintain the function of the polymerase. This may be the reason that the titer did not rebound to WT levels because the mutants are less fit.

Computational Assessment of the Bis-indole Induced Mutations on Inhibitors Binding to the RSV L Protein. We utilized the recently published cryo-EM structure of the RSV L bound to the RNA template to get insight into the possible mechanism of action of the bis-indole chemotype.[30] Interestingly, three of the mutated residues, namely M59, N224, and D575, are located in close proximity to the template

Scheme 3. Synthesis of Group B Bis-indole Derivatives 10a−e[a]

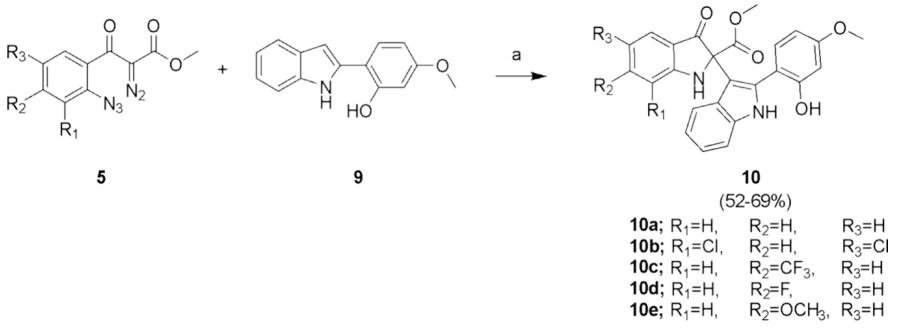

[a]Reagents and conditions: 10 mol % $Cu(OTf)_2$, DCM, rt.

https://doi.org/10.1021/acsomega.4c01207
ACS Omega 2024, 9, 22213−22229

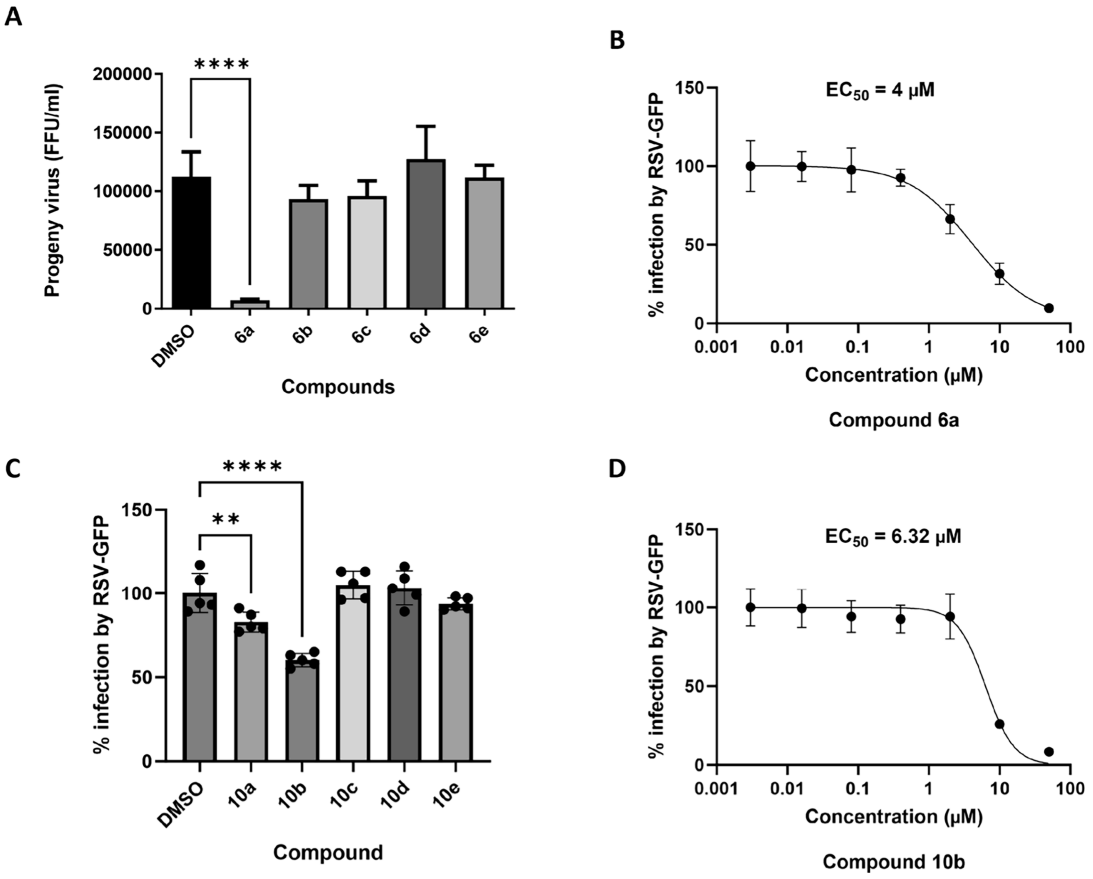

Figure 9. Effect of bis-indoles on RSV progeny production. (A) RSV viral progeny inhibition assay in the presence of the test compounds showing substantial inhibition of viral progeny in the presence of compound **6a** (**** $P < 0.0001$). Viral titers were performed in triplicate and expressed as focus-forming units (FFU/mL) and compounds were tested at 10 μM concentration. (B) Dose response curve of compound **6a** in RSV-GFP reporter assay. (C) Effect of group B compounds on viral infectivity. Viral expression is measured by GFP fluorescence 72 h postinfection. (D) Dose response curve of compound **10b** in RSV-GFP reporter assay measured 48 h postinfection. EC_{50} calculated through four-parameter variable slope regression modeling. Significance was determined by one-way ANOVA with Dunnett's test of significance vs DMSO controls, **$P = 0.0018$, ****$P < 0.0001$.

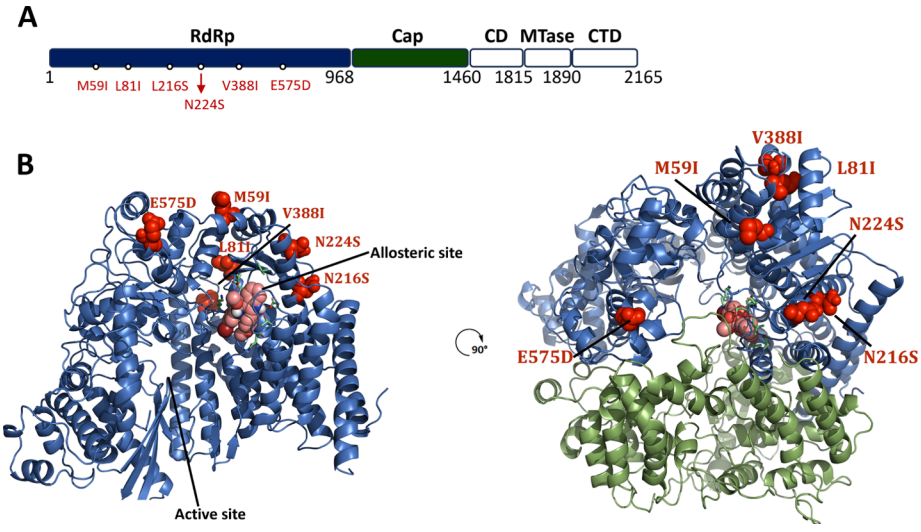

Figure 10. Resistance mutants in the RSV L protein associated with Bis-indole treatment. (A) Schematic representation of the RSV L domains with resistance sites for the bis-indole compounds mapped on the RdRp domain (domains are color coded). (B) 3D model of the RSV L protein showing sites of the resistant mutants (red spheres) and the allosteric binding sites. Mutations are clustered around the computationally identified allosteric binding site in the RSV L protein.

entry channel (Figure 11A). Moreover, residue N224 is located inside our identified pocket (Figure 11A). Based on this observation, we believe that the M59I and E575D mutations are compensatory mutations that are located near the template

https://doi.org/10.1021/acsomega.4c01207
ACS Omega 2024, 9, 22213−22229

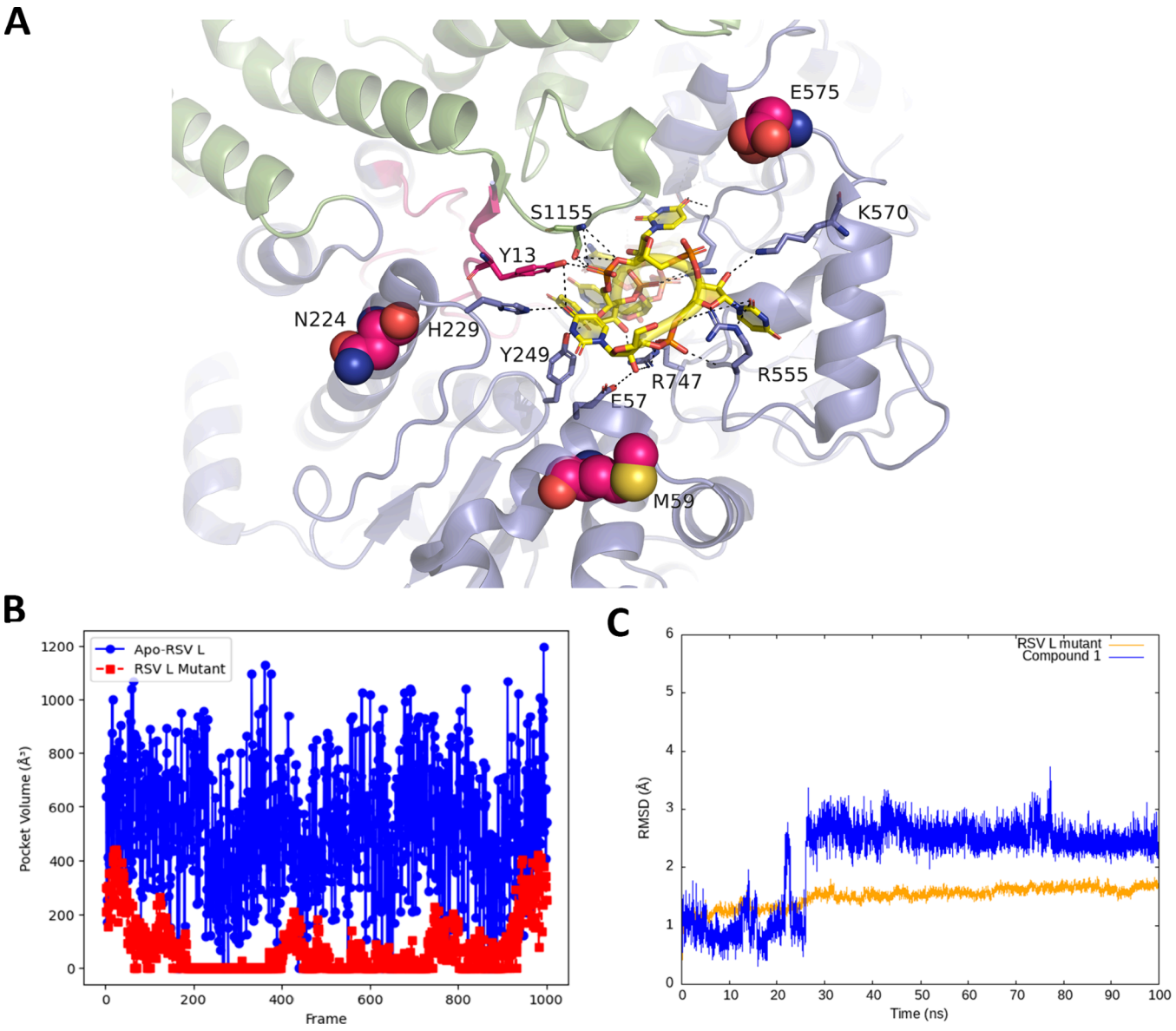

Figure 11. Effect of the bis-indole chemotype induced mutations on the RSV L allosteric site. (A) Schematic diagram of the cryo-EM structure of the RSV L bound to the RNA template (PDB ID: 8SNX). The figure was generated using PyMOL. Reproduced with permission from ref 30. Copyright 2023 Springer Nature. Residues mutated in response to compound **1** treatment are shown as spheres and the RNA is shown as yellow sticks with hydrogen bond interactions shown as black dotted lines. (B) MDpocket analysis of pocket 1 pocket volume change from the wild-type RSV L (blue) and the mutated RSV L (red) throughout the 100 ns MD trajectory (representative 1000 frames from the whole trajectory (10000 frames) were used for the analysis). (C) RMSD analysis of the trajectory showing the stability of the mutated protein (orange) and the ligand (blue) showing a drastic change in the ligand's RMSD from the starting coordinates.

entrance channel and may play a role in viral fitness restoration. This could rationalize the emergence of such mutations upon treatment with the bis-indole chemotype; however, a site-directed mutagenesis analysis will be performed to confirm this hypothesis.

To evaluate the impact of specific mutations on the binding of inhibitors to the allosteric pocket, all six mutations that emerged from compound **1** treatment were incorporated into the RSV L protein cryo-EM structure. Subsequently, a 100 ns MD simulation was conducted, and the resulting trajectory was subjected to clustering. The representative structure extracted from the lowest energy cluster was employed in a redocking experiment with compound **1**, the lead molecule tested in the viral evolution assay. Despite repeating the experiment with the same pocket coordinates, the analysis of the docked pose revealed that compound **1** exhibited negligible binding affinity to the allosteric pocket, indicated by a docking score of −3.4 kcal/mol.

One underlying assumption is that the introduced mutations in RSV L may have triggered conformational changes in the allosteric pocket. To assess this, a 100 ns MD simulation was performed on the apo-mutated RSV L protein, and the allosteric pocket's volume was monitored throughout the simulation. Intriguingly, the pocket volume exhibited a substantial reduction from approximately 517 Å to around 70 Å (Figure 11B). This reduction in pocket size could potentially explain why compound **1** might have difficulty binding effectively to this pocket.

To validate this finding, a 100 ns MD simulation was conducted for compound **1** bound to the mutated RSV L. As

https://doi.org/10.1021/acsomega.4c01207
ACS Omega 2024, 9, 22213−22229

anticipated, the compound failed to establish robust contacts and diffused away from the pocket after 20 ns of the simulation (Figure 11C and Movie S1). In summary, our MD simulations indicate that mutations induced by the bis-indole chemotype could lead to a conformational change in the allosteric pocket, resulting in a reduced pocket size. This alteration may adversely impact the druggability of the pocket, potentially contributing to the virus's enhanced ability to regain fitness. This result suggests that the bis-indole compounds were targeting the RSV L protein and were binding to a unique binding site in agreement with our computational model.

CONCLUSIONS

In this study, we utilized the published cryo-EM structures of the RSV L protein to structurally guide the design of a novel class of non-nucleoside polymerase inhibitors based on our previously discovered bis(indole) antivirals. A computational drug design approach has been employed to analyze the RSV L protein for possible druggable binding sites based on compound **1**. Our investigation led to the identification of an allosteric binding site located near the NTP entry site, and the stability of the residues lining this pocket was extensively investigated by MD simulations. Following a 100 ns MD simulation of the *apoprotein*, *in silico* screening of the two libraries based on the lead compound identified several residues that the compound can interact with and form a stable complex. We used our model to modify and optimize the lead compound, which eventually led to some modifications on the parent molecule. All the designed compounds have been ranked for their relative binding free energy using the MM/GBSA method to inform our synthesis decision and help rationalize SAR of this chemotype.

The antiviral activity of selected compounds represented both designed libraries has been screened *in vitro* for their ability to inhibit RSV infectivity. Among the tested compounds, compounds **6a** and **10b** showed the most promising antiviral activity, with EC_{50} values of 4 and 6.32 μM, respectively. This result agreed with our computational model regarding the possible binding site of this class of compounds, potentially leading to identifying a novel mechanism of viral protein inhibition. Viral resistant mutants emerged after incubation with escalating doses of the lead compound with the virus leading to mutations in the RdRp domain, which has not been associated with previously reported escape mutants from RSV allosteric inhibitors. This work serves as a starting point for the design and exploration of new chemical spaces as viral RdRp inhibitors with potentially novel mechanisms of viral protein inhibition. Future work will comprise isolation of the resistance mutants and further validation by measuring the fold change in EC_{50}'s associated with the treatment with the bis-indole moiety in both RSV A and RSV B subtypes.

EXPERIMENTAL SECTION

General Chemistry. Unless otherwise noted, all commercially available reagents were purchased and used without further purification unless otherwise noted. Flash chromatography columns were packed with 230−400 mesh silica gel (Silicycle). Nuclear magnetic resonance (NMR) spectra were obtained using Agilent/Varian VNMRS 400, 500, or 700 MHz spectrometers. For ^{1}H spectra, δ values were referenced to $CDCl_3$ (7.26 ppm) or DMSO-d_6 (2.49 ppm), and for the ^{13}C spectra, δ values were referenced to $CDCl_3$ (77.16 ppm) or DMSO-d_6 (39.5 ppm). Low-resolution mass was measured using Agilent Technologies 1100MSD LCMS (Single Quadruple) or Waters (Micromass) Q-TOF Premier LCMS/MS quadruple time-of-flight (TOF). High-resolution mass was measured using an Agilent Technologies 6220 orthogonal time-of-flight or Kratos Analytical MS-50G double focusing sector. The purity of the most active compounds was assessed by LC-UV (>95%).

Intermediate Preparation. The preparation of the β-keto ester intermediates was previously described.[22,43]

Representative Procedure for the Synthesis of compounds 5a−e. *Synthesis of Methyl 3-(2-Azidophenyl)-2-diazo-3-oxopropanoate (**5a**).* The title compounds were obtained following Scheme 1. For compound **5a**, 2-azidobenzoic acid (0.82 g, 5.0 mmol, 1 equiv) was added to a round-bottomed flask charged with DCM (35 mL) under a N_2 atmosphere and the suspension was cooled to 0 °C before the addition of trichloroacetyl chloride (0.70 mL, 6.0 mmol,1.20 equiv) followed by the addition of methyl acetate (0.40 mL, 6.0 mmol, 1.0 equiv). The solution was then transferred to a suspension of NaH (0.36 g, 15.0 mmol, 3 equiv) in DCM (10 mL) cooled at 0 °C. The solution was stirred at 0 °C for 15 min before being cooled to −45 °C followed by the addition of 1-methylimidazole (0.48 mL, 6.0 mmol, 1.2 equiv). After stirring for an additional 10 min at −45 °C, $TiCl_4$ (2.4 mL, 17.0 mmol, 3.4 equiv) was slowly added followed by Et_3N (2.8 mL, 20.0 mmol, 4.0 equiv). The reaction was kept at −45 °C for 45 min before being warmed up to 0 °C and kept at this temperature for an additional 1 h. The reaction was quenched with water, the organic layer was separated, and the aqueous layer was washed three times with dichloromethane. The combined organic layers were subsequently washed with water and brine, dried over $MgSO_4$, filtered, and concentrated under reduced pressure to furnish the crude mixture as an orange oil. The crude product was purified by flash chromatography (gradient 1 to 30% EtOAc in hexane) to afford 930 mg (85%) of the β-keto ester product **4a** as an orange oil; R_f = 0.60 (7:3 hexanes:EtOAc). The β-keto ester **4a** (900 mg, 4.11 mmol, 1.0 equiv) was then added to a stirred solution of triethylamine (0.70 mL, 4.93 mmol, 1.20 equiv) in CH_3CN (15 mL). Tosyl azide (0.90 mL, 4.11 mmol, 1.0 equiv) in CH_3CN (10 mL) was transferred via a cannula into the flask, and the reaction was stirred for 12 h. The reaction was monitored by TLC and LCMS for the formation of the new product, and upon reaction completion, the crude mixture was concentrated *in vacuo* followed by purification via flash chromatography (gradient elution 9:1 then 8:2 hexane/EtOAc) to afford the desired product **5a** as a yellow oil (910 mg, 67%); R_f = 0.46 (7:3 hexanes:EtOAc). ^{1}H NMR (500 MHz, $CDCl_3$) δ 7.48−7.41 (m, 1H), 7.26 (dd, J = 7.8, 1.6 Hz, 1H), 7.18−7.11 (m, 2H), 3.71 (s, 3H). ^{13}C NMR (126 MHz, $CDCl_3$) δ 185.7, 160.9, 137.8, 132.0, 130.4, 128.5, 124.8, 118.4, 52.4. (N.B.: The ^{13}C signal for the diazo carbon was not detected due to quadrupolar broadening.) HRMS (ESI) calcd for $C_{10}H_7N_5O_3$ $[M]^+$ 245.0549, found 245.0549.

*Methyl 3-(2-Azido-4-fluorophenyl)-2-diazo-3-oxopropanoate (**5b**).* The title compound was prepared analogously to **5a** starting from 2-azido-4-fluorobenzoic acid; isolated as reddish oil (200 mg, 62% yield from the β-keto ester intermediate **4b**); R_f = 0.56 (7:3 hexanes:EtOAc). ^{1}H NMR (700 MHz, $CDCl_3$) δ 7.32 (dd, J = 9.1, 5.9 Hz, 1H), 6.94−6.88 (m, 2H), 3.77 (s, 3H). ^{13}C NMR (176 MHz, $CDCl_3$) δ

https://doi.org/10.1021/acsomega.4c01207
ACS Omega 2024, 9, 22213−22229

184.7, 164.7 (d, J = 253.4 Hz), 160.9, 140.2 (d, J = 9.0 Hz), 130.7 (d, J = 9.9 Hz), 126.6 (d, J = 3.6 Hz), 112.3 (d, J = 22.1 Hz), 106.0 (d, J = 25.2 Hz), 52.5. (N.B.: The ^{13}C signal for the diazo carbon was not detected due to quadrupolar broadening.) HRMS (ESI) calcd for $C_{10}H_6FN_5O_3Na$ [M + Na] $^+$ 286.0347, found 286.0344.

*Methyl 3-(2-Azido-3,5-dichlorophenyl)-2-diazo-3-oxopropanoate (**5c**).* The title compound was prepared analogously to **5a** using 2-azido-3,5-dichlorobenzoic acid; isolated as a bright yellow oil (400 mg, 63% from the β-keto ester intermediate **4c**); R_f = 0.57 (7:3 hexanes:EtOAc). ^{1}H NMR (400 MHz, $CDCl_3$) δ 7.39 (d, J = 2.3 Hz, 1H), 7.31 (d, J = 2.4 Hz, 1H), 3.82 (s, 3H). ^{13}C NMR (101 MHz, $CDCl_3$) δ 185.5, 161.2, 143.4, 133.2, 129.9, 121.0, 119.8, 119.4, 52.7. (N.B.: the ^{13}C signal for the diazo carbon was not detected due to quadrupolar broadening.) HRMS (ESI) calcd for $C_{10}H_5Cl_2N_5O_3Na$ [M + Na] $^+$ 335.9662, found 335.9660.

*Methyl 3-(2-Azido-4-(trifluoromethyl)phenyl)-2-diazo-3-oxopropanoate (**5d**).* The title compound was prepared analogously to **5a** using 2-azido-4-(trifluoromethyl) benzoic acid; isolated as a red oil (50 mg, 46% from the β-keto ester intermediate **4d**); R_f = 0.50 (7:3 hexanes:EtOAc). ^{1}H NMR (500 MHz, $CDCl_3$) δ 7.45 (ddd, J = 7.9, 1.6, 0.8 Hz, 1H), 7.42−7.38 (m, 2H), 3.77 (s, 3H).13C NMR (126 MHz, $CDCl_3$) δ 184.8, 160.6, 138.7, 133.8 (q), 129.0, 124.0, 122.5, 121.7 (q), 115.4 (q), 52.6. (N.B.: The ^{13}C signal for the diazo carbon was not detected due to quadrupolar broadening.) HRMS (ESI) calcd for $C_{11}H_6F_3N_5O_3Na$ [M + Na]$^+$ 336.0315, found 336.0316.

*Methyl 3-(2-Azido-4-chlorophenyl)-2-diazo-3-oxopropanoate (**5e**).* The title compound was prepared analogously to **5a** using 2-azido-4-chlorobenzoic acid; isolated as a yellow oil (1.5 g, 62% from the β-keto ester intermediate **4e**); R_f = 0.69 (7:3 hexanes:EtOAc). ^{1}H NMR (500 MHz, $CDCl_3$) δ 7.26−7.21 (m, 1H), 7.16 (d, J = 6.8 Hz, 2H), 3.76 (s, 3H). ^{13}C NMR (126 MHz, $CDCl_3$) δ 184.7, 160.8, 139.2, 137.8, 129.7, 128.8, 125.2, 118.6, 52.4. (N.B.: the ^{13}C signal for the diazo carbon was not detected due to quadrupolar broadening.) HRMS (ESI) calcd for $C_{10}H_6ClN_5O_3Na$ [M + Na] $^+$ 302.0051, found 302.0051.

Representative Procedure for the Synthesis of the Bis-indole Compounds (6a−e and 10a−e). *Synthesis of Methyl 2-(5-Hydroxy-1H-indol-3-yl)-3-oxoindoline-2-carboxylate (**6a**).* To an oven-dried round-bottomed flask, a solution of 5-hydroxy indole (221 mg, 0.60 mmol) in DCM (25 mL) and Cu(OTf)$_2$ (6.50 mg, 0.031 mmol) was stirred for 5 min followed by the addition of a solution of diazo-azide **5a** (75 mg, 0.31 mmol) via a syringe pump over 1 h at room temperature. Once the addition was completed, the reaction was monitored by TLC for consumption of starting material **5a**. After 24 h, the starting material was completely consumed, and the reaction mixture was concentrated under reduced pressure and purified by flash chromatography (silica gel, gradient elution 8:2 then 7:3 hexane/EtOAc) to afford the bis-indole product **6a** as a yellow oil (90 mg, 91%); R_f = 0.24 (7:3 hexanes:EtOAc). ^{1}H NMR (500 MHz, $CDCl_3$) δ 8.08 (s, 1H), 7.69 (d, J = 7.8 Hz, 1H), 7.53 (ddd, J = 8.3, 7.1, 1.4 Hz, 1H), 7.37 (d, J = 2.7 Hz, 1H), 7.22 (dd, J = 8.7, 0.6 Hz, 1H), 7.03−6.97 (m, 2H), 6.93 (ddd, J = 7.9, 7.1, 0.8 Hz, 1H), 6.78 (dd, J = 8.7, 2.4 Hz, 1H), 5.69 (s, 1H), 4.55 (s, 1H), 3.81 (s, 3H). ^{13}C NMR (126 MHz, $CDCl_3$) δ 194.6, 168.9, 161.0, 149.9, 137.9, 131.8, 126.1, 125.4, 124.5, 120.4, 119.9, 113.6, 112.6, 112.3, 111.0, 104.2, 72.4, 53.8. HRMS (ESI) calcd for $C_{18}H_{13}N_2O_4$ [M-H]$^-$ 321.0881; found 321.0879.

*Methyl 6-Fluoro-2-(5-hydroxy-1H-indol-3-yl)-3-oxoindoline-2-carboxylate (**6b**).* The title compound was prepared analogously to **6a** but using (0.16 mmol) of **5a**, and the product was purified by flash chromatography following the previously mentioned procedure and was isolated as yellow oil in 73% yield; R_f = 0.22 (7:3 hexanes:EtOAc). ^{1}H NMR (500 MHz, $CDCl_3$) δ 8.12 (s, 1H), 7.68 (ddd, J = 9.1, 5.7, 0.7 Hz, 1H), 7.36 (d, J = 2.9 Hz, 1H), 7.23 (dd, J = 8.7, 0.6 Hz, 1H), 7.02−6.91 (m, 2H), 6.82−6.76 (m, 1H), 6.63 (ddd, J = 8.9, 6.8, 2.1 Hz, 2H), 5.80 (s, 1H), 3.82 (s, 3H). ^{13}C NMR (126 MHz, $CDCl_3$) δ 192.7, 168.8 (d, J = 5.8 Hz), 162.5 (d, J = 14.1 Hz), 150.1, 131.9, 128.9, 127.9 (d, J = 12.4 Hz), 12.50, 126.1, 124.6, 116.3, 112.6 (d, J = 42.3 Hz), 110.8, 109.2 (d, J = 24.7 Hz), 104.21, 100.0 (d, J = 26.0 Hz), 73.0, 54.0. HRMS (ESI) calcd for $C_{18}H_{12}FN_2O_4$ [M-H]$^-$ 339.0787; found 339.0787.

*Methyl 5,7-Dichloro-2-(5-hydroxy-1H-indol-3-yl)-3-oxoindoline-2-carboxylate (**6c**).* The title compound was prepared analogously to **6a** but using (0.14 mmol) of **5c** instead of **5a**, and the product was isolated as yellow oil in 84% yield; R_f = 0.20 (7:3 hexanes:EtOAc). ^{1}H NMR (500 MHz, $CDCl_3$) δ 8.14 (s, 1H), 7.55 (dd, J = 12.6, 2.0 Hz, 2H), 7.35 (d, J = 2.8 Hz, 1H), 7.23 (d, J = 8.7 Hz, 1H), 7.01 (d, J = 2.4 Hz, 1H), 6.80 (dd, J = 8.7, 2.4 Hz, 1H), 5.83 (s, 1H), 3.83 (s, 3H). ^{13}C NMR (126 MHz, $CDCl_3$) δ 192.8, 167.8, 155.6, 150.0, 136.4, 131.8, 125.7, 125.5, 124.5, 123.2, 121.6, 119.2, 112.8, 112.4, 109.9, 104.2, 73.3, 54.0. HRMS (ESI) calcd for $C_{18}H_{12}Cl_2N_2O4$ [M + H]$^+$ 389.0101; found 389.0095.

*Methyl 2-(5-Hydroxy-1H-indol-3-yl)-3-oxo-6-(trifluoromethyl)indoline-2-carboxylate (**6d**).* The title compound was carried out on a small scale (18 mg, 0.060 mmol of the intermediate **5d**), prepared and purified analogously to **6a**, and the product was isolated as yellow oil in 68% yield; R_f = 0.24 (7:3 hexanes:EtOAc). ^{1}H NMR (500 MHz, $CDCl_3$) δ 8.11 (s, 1H), 7.78 (d, J = 8.1 Hz, 1H), 7.36 (d, J = 2.8 Hz, 1H), 7.24 (d, J = 8.8 Hz, 2H), 7.15 (d, J = 5.2 Hz, 1H), 7.08−6.94 (m, 2H), 6.80 (dd, J = 8.7, 2.4 Hz, 1H), 5.86 (s, 1H), 3.82 (s, 3H).HRMS (ESI) calcd for $C_{19}H_{13}F_3N_2O_4Na$ [M + Na]$^+$ 413.0720; found 413.0720. (Due to the small scale of the reaction, no ^{13}C data was obtained.)

*Methyl 6-Chloro-2-(5-hydroxy-1H-indol-3-yl)-3-oxoindoline-2-carboxylate (**6e**).* The title compound was prepared analogously to **6a** but using (1.7 mmol) of **5e** instead of **5a**, and the product was isolated as yellow oil in 98% yield; R_f = 0.22 (7:3 hexanes:EtOAc). ^{1}H NMR (700 MHz, $CDCl_3$) δ 8.11 (s, 1H), 7.60 (d, J = 8.4 Hz, 1H), 7.35 (d, J = 2.7 Hz, 1H), 7.22 (d, J = 8.7 Hz, 1H), 6.98 (dd, J = 3.8, 2.0 Hz, 3H), 6.89 (dd, J = 8.2, 1.7 Hz, 1H), 6.79 (dd, J = 8.7, 2.4 Hz, 1H), 5.75 (s, 1H), 3.82 (s, 3H). ^{13}C NMR (176 MHz, $CDCl_3$): δ 192.9, 168.0, 155.8, 150.1, 136.5, 131.9, 125.9, 125.6, 124.6, 123.4, 121.7, 119.4, 112.9, 112.5, 110.0, 104.3, 73.4, 54.1. HRMS (ESI) calcd for $C_{18}H_{14}ClN_2O_4$ [M + H] $^+$ 357.0637; found 357.064.

*2-(1H-Indol-2-yl)-5-methoxyphenol (**9**).* Phenyl hydrazine (3.0 mL, 30.0 mmol) was added to a stirred solution of 2′-hydroxy-4′-methoxyacetophenone (5.0 g, 30.0 mmol) in absolute EtOH (30 mL), followed by 5 drops of HOAc. The reaction mixture was heated at 80 °C for 1 h. The reaction was allowed to cool to rt, and then the solvent was removed under reduced pressure. Polyphosphoric acid (PPA, 10 mL) was added to the residue, and the mixture was heated slowly to 130 °C and kept at this temperature for 1 h. The reaction mixture

https://doi.org/10.1021/acsomega.4c01207
ACS Omega 2024, 9, 22213−22229

was poured onto ice and neutralized with 2 M NaOH. After neutralization, the greyish solid formed was filtered, washed with water (3 × 100 mL), and purified by flash chromatography (gradient 5 to 20% EtOAc in hexane) to afford the desired compound **9** as yellow-gray solid (4.9 g, 68%). ^{1}H NMR (500 MHz, DMSO-d_6) δ 10.96 (s, 1H), 10.20 (s, 1H), 7.65 (d, J = 8.6 Hz, 1H), 7.46 (dd, J = 7.8, 1.2 Hz, 1H), 7.41 (dd, J = 8.0, 1.0 Hz, 1H), 7.01 (ddd, J = 8.1, 6.9, 1.2 Hz, 1H), 6.94 (ddd, J = 8.0, 7.0, 1.1 Hz, 1H), 6.82 (d, J = 0.9 Hz, 1H), 6.56 (d, J = 2.5 Hz, 1H), 6.52 (dd, J = 8.6, 2.6 Hz, 1H), 3.75 (s, 3H). ^{13}C NMR (126 MHz, DMSO-d_6) δ 159.4, 155.5, 136.0, 135.5, 128.4, 128.3, 120.4, 119.2, 118.7, 112.1, 111.0, 105.3, 101.8, 99.2, 55.0. HRMS (ESI) calcd for $C_{15}H_{13}O_2$ [M-H]$^-$ 238.0874; found 238.0872.

*Methyl 2-(2-(2-hydroxy-4-methoxyphenyl)-1H-indol-3-yl)-3-oxoindoline-2-carboxylate (**10a**).* The title compound was prepared analogously to **6a** but using 2.0 equiv of compound **9** in place of 5-hydroxy indole and (0.017 mmol) of **5a**. Compound **10a** was isolated as yellow semisolid in 52% yield; R_f = 0.31 (7:3 hexanes:EtOAc). ^{1}H NMR (500 MHz, $CDCl_3$) δ 8.07 (s, 1H), 7.63 (dd, J = 7.8, 1.3 Hz, 1H), 7.57 (ddd, J = 8.4, 7.1, 1.4 Hz, 1H), 7.35−7.29 (m, 2H), 7.18 (ddd, J = 8.1, 7.1, 1.1 Hz, 1H), 7.13 (d, J = 8.4 Hz, 1H), 7.04−6.90 (m, 3H), 6.56 (d, J = 2.5 Hz, 1H), 6.52 (dd, J = 8.4, 2.5 Hz, 1H), 5.69 (s, 1H), 3.80 (s, 3H), 3.29 (s, 3H). (N.B.: The ^{1}H signal for the phenolic proton was not detected). ^{13}C NMR (126 MHz, CDCl3) δ 196.6, 168.3, 162.1, 160.8, 156.8, 138.3, 135.6, 132.3, 131.8, 126.1, 125.6, 122.9, 120.5, 120.5, 119.8, 119.3, 113.1, 111.2, 111.0, 110.3, 106.8, 102.1, 73.3, 55.4, 53.3. HRMS (ESI) calcd for $C_{25}H_{20}N_2O_5Na$ [M + Na]$^+$ 451.1264; found 451.1257.

*Methyl 5,7-Dichloro-2-(2-(2-hydroxy-4-methoxyphenyl)-1H-indol-3-yl)-3-oxoindoline-2-carboxylate (**10b**).* The title compound was prepared analogously to **10a**, and the product was isolated as yellow oil in 67% yield; R_f = 0.40 (7:3 hexanes:EtOAc). ^{1}H NMR (500 MHz, $CDCl_3$) δ 8.11 (s, 1H), 7.57−7.51 (m, 1H), 7.48 (dd, J = 2.0, 0.7 Hz, 1H), 7.38−7.32 (m, 1H), 7.28−7.19 (m, 2H), 7.14−7.03 (m, 2H), 6.56−6.49 (m, 2H), 3.81 (s, 3H), 3.38 (s, 3H). (N.B.: The ^{1}H signals for the phenolic and indolinone protons were not detected). ^{13}C NMR (126 MHz, $CDCl_3$) δ 194.6, 167.6, 162.4, 156.5, 155.5, 136.7, 135.7, 132.3, 131.9, 126.1, 125.6, 123.3, 123.3, 121.3, 120.9, 119.6, 119.0, 111.4, 110.9, 109.8, 107.1, 102.0, 74.1, 55.6, 53.7. HRMS (ESI) calcd for $C_{25}H_{18}Cl_2N_2O_5Na$ [M + Na]$^+$ 519.0485; found 518.0482.

*Methyl 2-(2-(2-Hydroxy-4-methoxyphenyl)-1H-indol-3-yl)-3-oxo-6 (trifluoromethyl)indoline-2-carboxylate (**10c**).* The title compound was prepared analogously to **10a** but using (0.060 mmol) of **5d** instead of **5a**, and the product was isolated as yellow oil in 58% yield; R_f = 0.35 (7:3 hexanes:EtOAc). ^{1}H NMR (500 MHz, $CDCl_3$) δ 8.09 (s, 1H), 7.74−7.68 (m, 1H), 7.35 (dt, J = 8.2, 0.9 Hz, 1H), 7.28 (dd, J = 8.1, 0.9 Hz, 1H), 7.23−7.20 (m, 2H), 7.16−7.09 (m, 2H), 7.08−7.01 (m, 1H), 6.96 (s, 1H), 6.54 (d, J = 2.5 Hz, 1H), 6.51 (dd, J = 8.4, 2.5 Hz, 1H), 5.84 (s, 1H), 3.81 (s, 3H), 3.35 (s, 3H). HRMS (ESI) calcd for $C_{26}H_{19}F_3N_2O_5Na$ [M + Na]$^+$ 519.1138; found 519.1133. (Due to the small scale of the reaction, no ^{13}C data was obtained.)

*Methyl 6-Fluoro-2-(2-(2-hydroxy-4-methoxyphenyl)-1H-indol-3-yl)-3-oxoindoline-2-carboxylate (**10d**).* The title compound was prepared analogously to **10a** but using (0.18 mmol) of **5d** instead of **5a**, and the product was isolated as yellow oil in 58% yield; R_f = 0.30 (7:3 hexanes:EtOAc). ^{1}H NMR (500 MHz, $CDCl_3$) δ 8.06 (s, 1H), 7.66−7.60 (m, 1H), 7.37−7.28 (m, 3H), 7.23−7.16 (m, 1H), 7.13 (d, J = 8.4 Hz, 1H), 7.06−6.99 (m, 1H), 6.64 (dd, J = 9.1, 7.5 Hz, 2H), 6.57 (d, J = 2.5 Hz, 1H), 6.53 (dd, J = 8.4, 2.5 Hz, 1H), 5.79 (s, 1H), 3.81 (s, 3H), 3.30 (s, 3H). ^{13}C NMR (126 MHz, $CDCl_3$) 194.6, 168.1, 162.3 (d, J = 3.3 Hz), 156.9, 135.7, 132.4, 131.9, 128.2 (d, J = 12.5 Hz), 126.1, 123.2, 120.7, 119.8, 115.9, 111.2 (d, J = 4.1 Hz), 110.1, 109.3 (d, J = 24.7 Hz), 107.0, 102.3, 99.6 (d, J = 26.2 Hz), 74.0, 55.5, 53.5. (N.B.: Three carbon resonance ^{13}C were missing and could not be properly assigned.) HRMS (ESI) calcd for $C_{25}H_{18}FN_2O_5$ [M-H]$^-$ 445.1205; found 445.1194.

*Methyl 2-(2-(2-Hydroxy-4-methoxyphenyl)-1H-indol-3-yl)-6-methoxy-3-oxoindoline-2-carboxylate (**10e**).* The title compound was prepared analogously to **10a** but using (2.0 mmol) of **5e** instead of **5a**, and the product was isolated as yellow oil in 69% yield; R_f = 0.30 (7:3 hexanes:EtOAc). ^{1}H NMR (500 MHz, $CDCl_3$) δ 8.03 (s, 1H), 7.55 (d, J = 8.7 Hz, 1H), 7.37−7.30 (m, 2H), 7.21−7.11 (m, 2H), 7.00 (ddd, J = 8.2, 7.1, 1.0 Hz, 1H), 6.59 (d, J = 2.5 Hz, 1H), 6.52 (td, J = 8.6, 2.3 Hz, 2H), 6.41 (d, J = 2.1 Hz, 1H), 5.69 (s, 1H), 3.90 (s, 3H), 3.81 (s, 3H), 3.25 (s, 3H). (N.B.: The ^{1}H signal for the phenolic proton was not detected). ^{13}C NMR (126 MHz, $CDCl_3$) δ 194.3, 168.8, 168.6, 163.3, 162.2, 157.3, 135.7, 132.4, 131.9, 127.3, 126.2, 123.0, 120.6, 120.0, 112.7, 111.5, 111.1, 110.5, 106.9, 102.5, 95.3, 73.9, 55.9, 55.5, 53.3. HRMS (ESI) calcd for $C_{26}H_{22}N_2O_6Na$ [M + Na]$^+$ 481.1370; found 481.1370.

Computational Details. *Preparation of the Target Protein for MD Simulations.* The cryo-electron microscopy structure of the RSV L protein bound to the tetrameric P protein (PDB ID: 6PZK), which has a resolution of 3.20 Å, was used for our study. Initially, we started by building up the missing loop residues (609−626) using Prime implemented in the Schrödinger Small Molecule Discovery Suite.[32,44] For the mutated protein, mutations were introduced also using the Schrödinger Small Molecule Discovery Suite, and the structure was minimized using the Protein Preparation Wizard before being prepared for the MD simulations.

The Protein Preparation Wizard module was used to add hydrogen atoms, minimize energy, and create appropriate protonation states for amino acid side chains and was then subjected to three stages of energy minimization. The AMBERff14SB force field parameters were assigned to the protein.[45] The protein was then solvated in a cubic box of TIP3P water.[46] The solvated system was then neutralized with the addition of Na^+/Cl^- counterions at a concentration of 0.15 M physiological ionic concentration using leap in AmberTools20. The system was then carried forward for subsequent MD simulation. Details on the MD simulations are discussed below.

Binding Site Identification. MD simulation trajectories for the RSV L protein were used to identify potential allosteric pockets. Three different tools were employed to search for those pockets, including fPocket,[25] Site Finder implemented in MOE,[47] and the SiteMap utility implemented in Schrödinger[26] and the MDpocket script[33] on the MD trajectory of the *apo* protein. Agreement between these tools regarding pocket size and druggability scores along with the pocket volume obtained from the MD simulations were the main criteria for pocket selection.

Molecular Docking. The 2D chemical structures of the ligands were built using ChemDraw version 19.0, and the

https://doi.org/10.1021/acsomega.4c01207
ACS Omega 2024, 9, 22213−22229

structures were prepared using the LigPrep wizard implemented in Schrödinger. Protonation states at pH 7.0 ± 2.0 for each ligand were assigned using Epik and the ligands' tautomer and conformations were calculated using the OPLS3e force field.[48,49] The docking grid box was defined in the center of residues N895, D899, D16, K20, and K1145 with center coordinates of 149.41, 118.59, and 140.67. The Glide scoring function at extra precision (XP) was used for the docking simulations. A maximum of 10 poses were generated for each compound, and the top-scoring pose was selected for each ligand.

MD Simulations and MM-GBSA Rescoring. Complexes preparation followed the above-described method. The force field parameters for the ligands were obtained using the GAFF force field[50] and Antechamber,[51] and the AM1-BCC charges were assigned for the ligands.[52] The MD simulations were performed using the AMBER20 molecular dynamics package[53] with pmemd.cuda: initial minimization steps were performed in order to relax the water and ionic positions using 1000 steps of the steepest descent and 1000 steps of conjugate gradients minimization, keeping all the complex atoms fixed through a harmonic restraint with a force constant of 500 kcal/mol/Å^2. This step was followed by 2000 steps of the steepest descent followed by 3000 steps of conjugate gradients without restraints. The systems were then heated gradually up from 0 to 300 K in 100 ps using Langevin dynamics.[54] During the heating process, the backbone of the protein and the heavy atoms of the ligand were restrained, and a time step of 0.5 fs and periodic volume conditions were employed during this phase. The time step has been set to 2 fs, and periodic pressure conditions (1 atm) have been imposed and the restraints have been gradually released in four phases of 50 ps each. The simulations were then continued for 100 ns of production. Analysis of the MD trajectory was carried out using CPPTRAJ.[55] Plots were generated using Gnuplot (version 5.4), Matplotlib, and figures were generated using PyMol.

For MD snapshots extracted from the production simulations, we calculated the enthalpic portion of the binding energy using the molecular mechanics/generalized Born surface area (MM/GBSA) method implemented in the MMPBSA.py script.[56] In MM/GBSA, the free energy change due to ligand binding is calculated as

$$\Delta G_{\text{bind}} = \Delta E_{\text{MM}} + \Delta G_{\text{solv}} - T\Delta S \quad (1)$$

where ΔE_{MM}, is the summation of nonbonded and bonded interaction energies. The solvation energy, ΔG_{solv}, is the sum of the polar and nonpolar contributions of solvation, where the polar solvation terms are calculated using a generalized Born model (igb = 5) and the nonpolar terms are computed based on the size of the solvent-accessible surface area. The ($T\Delta S$) portion of the equation refers to the entropic contribution and is computationally expensive and, therefore, is neglected. The pairwise decomposition analysis (idecomp = 4) using the MD trajectories were also carried out to identify the key ligand−residue energetic contributors to the binding free energy of the complexes.

Virological Assays. *Cells and Virus.* Henrietta Lack's (HeLa) cells from American Type Culture Collection (ATCC, CCL2) were grown in Dulbecco's modified Eagle's medium (DMEM) containing L-glutamine, glucose, and sodium pyruvate with 10% heat inactivated fetal bovine serum (FBS). Human airway epithelial (1HAEo-) cells were grown in minimum essential medium (MEM) supplemented with 10% heat inactivated FBS. All cell lines were incubated at 37 °C with 5% CO_2.

Compound Evaluation and Infectious RSV Quantification. Confluent 1HAEo- cells were preincubated with the compounds for 1 h at 10 μM, followed by infection with RSV-A2-GFP at an MOI of 1 for 2 h. At 2 h postinfection, the infectious medium was removed from wells to prevent the carryover of infectious virus into progeny collections. Cells were fixed and permeabilized with methanol: acetone (1:1), blocked with PBS + 5% FBS, and stained with goat polyclonal anti-RSV antibody (1:1000 dilution), followed by the addition of an antigoat secondary antibody conjugated to β-galactosidase (1:2000 dilution). Infected cells were stained blue upon the addition of X-Gal substrate (5-bromo-4-chloro-3-indoyl-β-galactopyranoside) in PBS containing 3 mM potassium ferricyanide, 3 mM potassium ferrocyanide and 1 mM magnesium chloride. The cleavage of the X-Gal substrate by β-galactosidase generates an insoluble blue precipitate which indicates RSV infection. Blue stained cells were manually counted as RSV focus-forming units by light microscopy using the EVOS FL Auto Cell Imaging System (Invitrogen).

RSV A2-GFP Viral Replication Assays. HeLa cells were plated at a concentration of 2×10^4 cells per well in a black 96-well tray with clear bottom to observe the health of the cells. The next day, replicate wells were pretreated with drug for 30 min and then infected with low passage RSV-GFP at an MOI of 0.2. At 4 h post infection, the growth media was changed to fresh 1x drug and the cells were allowed to incubate at 37 °C, 5% CO2 for 48 h. The media was then removed and clear DMEM was added before reading GFP fluorescence on the Promega GloMax Explorer, Ex: 475 nm, Em: 500−550 nm.

Viral Escape Mutant Assay. Compound **1** at concentrations 10 μM and 25 μM was diluted in DMSO and incubated with lab strain rgRSV A2 at an MOI of 0.5 in subconfluent HeLa cells. After 4 h post infection, fresh media containing the compound was added to the cells and the infection was allowed to proceed at 37 °C, 5% CO_2. After 48 h, virus-conditioned media was clarified and then a portion was used to infect a new HeLa cell monolayer in the presence of the compound again to repeat the process. The viruses were passaged 20 times with the respective compound. RNA was harvested for every passage and viral growth was measured by qRT-PCR and a foci counting assay to test infectivity.

Whole Genome Sequencing. Whole genome sequencing was done as described previously.[57] Briefly, viral RNA from each passage of the evolution experiment was extracted using the QIAamp Viral RNA Mini Kit (Qiagen, 52906). Viral mRNA was isolated by poly-A pulldown with oligo d(T) 25 beads using the NEBNext Poly(A) mRNA Magnetic Isolation Module (NEB, E7490L). The first strand of cDNA was prepared using the High-Capacity cDNA RT Kit (ThermoFisher, 4368814), and the second strand was synthesized with the large Klenow fragment of DNA polymerase 1 (NEB, M0210L). cDNA was purified with the MinElute PCR purification kit (Qiagen, 28004). Tagmentation and creation of the library was done using the Nextera XT DNA Library Preparation Protocol (Illumina, FC-131−1096). Index adapters used for sample identification were created by MBSU (Molecular Biology Service Unit, University of Alberta, Edmonton, AB, Canada), and libraries were cleaned up using the MagJET NGS Cleanup Kit (ThermoFisher, K2821). Sample concentration was checked using the NanoDrop

https://doi.org/10.1021/acsomega.4c01207
ACS Omega 2024, 9, 22213−22229

8000 spectrophotometer (ThermoFisher, ND-8000-GL), and sample purity was analyzed by the Agilent 2100 Bioanalyzer G2938C (Marshall Scientific, AG-2100C) at the MBSU. Equal amounts of DNA were combined and sent for sequencing to the MBSU for Next Generation Sequencing on the MiSeq System (Illumina, SY-410−1003).

Statistical Analysis. GraphPad Prism software version 10.0.1 was used for all statistical analyses. Significance was determined by one-way ANOVA with Dunnett's test of significance vs DMSO. Fifty percent maximal effective concentrations (EC_{50}) were calculated using four-parameter nonlinear regression modeling.

■ ASSOCIATED CONTENT

Supporting Information

The Supporting Information is available free of charge at https://pubs.acs.org/doi/10.1021/acsomega.4c01207.

Surface electrostatic potential of the RSV L-P complex; trajectory analysis of the RSV L-P apoprotein; virtual screening library; sequence alignment of negative-stranded viruses; summary of docking and MM/GBSA results; pair-residue decomposition analysis; RSV viral evolution titers; ^{1}H and ^{13}C spectra for key intermediates and final compounds; and LC-UV purity assessment for compounds **6a** and **10b** (PDF)

(Movie S1) MD simulation of compound **1** in complex with the mutated RSV L; the compound diffused away from the binding pocket after 20 ns of the simulation (MP4)

■ AUTHOR INFORMATION

Corresponding Authors

Frederick G. West − *Department of Chemistry, University of Alberta, Edmonton, Alberta T6G 2G2, Canada;* orcid.org/0000-0001-7419-2314; Email: fwest@ualberta.ca

David J. Marchant − *Department of Medical Microbiology and Immunology, University of Alberta, Edmonton, AB T6G 2R3, Canada;* orcid.org/0009-0007-1783-0448; Email: marchant@ualberta.ca

Authors

Ahmed K. Oraby − *Department of Medical Microbiology and Immunology, University of Alberta, Edmonton, AB T6G 2R3, Canada; Department of Chemistry, University of Alberta, Edmonton, Alberta T6G 2G2, Canada; Department of Pharmaceutical Organic Chemistry, College of Pharmaceutical Sciences and Drug Manufacturing, Misr University for Science and Technology, 6th of October City 77, Egypt;* orcid.org/0000-0001-5546-6703

Leanne Bilawchuk − *Department of Medical Microbiology and Immunology, University of Alberta, Edmonton, AB T6G 2R3, Canada*

Complete contact information is available at: https://pubs.acs.org/10.1021/acsomega.4c01207

Author Contributions

All authors have given approval to the final version of the manuscript. A.K.O. designed and wrote the manuscript, performed the computational studies, synthesized, and characterized all the compounds. L.B. performed the antiviral screening. F.G.W. and D.J.M. acquired funding, supervised the work, and drafted the manuscript.

Notes

The authors declare the following competing financial interest(s): The authors declare the following conflict of interest. A.K.O, L.B., F.G.W, and D.J.M. are inventors on U.S. patent application no. (63/631,132) describing the compounds and their method of use.

■ ACKNOWLEDGMENTS

This research was enabled in part by the support provided by a project grant from the Canadian Institutes for Health Research, an operating grant from Striving for Pandemic Preparedness − The Alberta Research Consortium (SPP-ARC), and the Digital Research Alliance of Canada (alliancecan.ca) for computational resources.

■ ABBREVIATIONS

RdRp, RNA-dependent RNA polymerase; OPLS, optimized potentials for liquid simulations; MD, molecular dynamics; SAR, structure−activity relationship; MM/GBSA, molecular mechanics generalized Born surface area; GFP, green fluorescent protein; rgRSV, reverse engineered respiratory syncytial virus

■ REFERENCES

(1) Collins, P. L.; Graham, B. S. Viral and Host Factors in Human Respiratory Syncytial Virus Pathogenesis. *J. Virol.* **2008**, *82* (5), 2040.

(2) Hall, C. B.; Weinberg, G. A.; Iwane, M. K.; Blumkin, A. K.; Edwards, K. M.; Staat, M. A.; Auinger, P.; Griffin, M. R.; Poehling, K. A.; Erdman, D.; et al. The burden of respiratory syncytial virus infection in young children. *N Engl J. Med.* **2009**, *360* (6), 588−598.

(3) Falsey, A. R.; Hennessey, P. A.; Formica, M. A.; Cox, C.; Walsh, E. E. Respiratory syncytial virus infection in elderly and high-risk adults. *N Engl J. Med.* **2005**, *352* (17), 1749−1759.

(4) Resch, B. Burden of respiratory syncytial virus infection in young children. *World journal of clinical pediatrics* **2012**, *1* (3), 8−12.

(5) Piedimonte, G.; Perez, M. K. Respiratory syncytial virus infection and bronchiolitis. *Pediatr. Rev.* **2014**, *35* (12), 519−530.

(6) Pérez-Yarza, E. G.; Moreno, A.; Lázaro, P.; Mejías, A.; Ramilo, O. The association between respiratory syncytial virus infection and the development of childhood asthma: a systematic review of the literature. *Pediatr Infect Dis J.* **2007**, *26* (8), 733−739.

(7) Xu, L.; Gao, H.; Zeng, J.; Liu, J.; Lu, C.; Guan, X.; Qian, S.; Xie, Z. A fatal case associated with respiratory syncytial virus infection in a young child. *BMC Infect. Dis.* **2018**, *18* (1), 217.

(8) Papi, A.; Ison, M. G.; Langley, J. M.; Lee, D. G.; Leroux-Roels, I.; Martinon-Torres, F.; Schwarz, T. F.; van Zyl-Smit, R. N.; Campora, L.; Dezutter, N.; et al. Respiratory Syncytial Virus Prefusion F Protein Vaccine in Older Adults. *N Engl J. Med.* **2023**, *388* (7), 595−608.

(9) Blount, R. E., Jr.; Morris, J. A.; Savage, R. E. Recovery of cytopathogenic agent from chimpanzees with coryza. *Proc. Soc. Exp Biol. Med.* **1956**, *92* (3), 544−549.

(10) Wegzyn, C.; Toh, L. K.; Notario, G.; Biguenet, S.; Unnebrink, K.; Park, C.; Makari, D.; Norton, M. Safety and Effectiveness of Palivizumab in Children at High Risk of Serious Disease Due to Respiratory Syncytial Virus Infection: A Systematic Review. *Infect Dis Ther* **2014**, *3* (2), 133−158.

(11) Hammitt, L. L.; Dagan, R.; Yuan, Y.; Baca Cots, M.; Bosheva, M.; Madhi, S. A.; Muller, W. J.; Zar, H. J.; Brooks, D.; Grenham, A.; et al. Nirsevimab for Prevention of RSV in Healthy Late-Preterm and Term Infants. *N Engl J. Med.* **2022**, *386* (9), 837−846.

(12) Turner, T. L.; Kopp, B. T.; Paul, G.; Landgrave, L. C.; Hayes, D., Jr.; Thompson, R. Respiratory syncytial virus: current and emerging treatment options. *ClinicoEconomics and outcomes research: CEOR* **2014**, *6*, 217−225.

(13) Jeffree, C. E.; Rixon, H. W. M.; Brown, G.; Aitken, J.; Sugrue, R. J. Distribution of the attachment (G) glycoprotein and GM1 within the envelope of mature respiratory syncytial virus filaments revealed using field emission scanning electron microscopy. *Virology* **2003**, *306* (2), 254−267.
(14) Fields, B. N.; Knipe, D. M.; Howley, P. M. *Fields virology*; Wolters Kluwer Health/Lippincott Williams & Wilkins, 2013.
(15) Hacking, D.; Hull, J. Respiratory syncytial virus: viral biology and the host response. *J. Infect* **2002**, *45* (1), 18−24.
(16) Morin, B.; Kranzusch, P. J.; Rahmeh, A. A.; Whelan, S. P. J. The polymerase of negative-stranded RNA viruses. *Current Opinion in Virology* **2013**, *3* (2), 103−110.
(17) Collins, P. L.; Fearns, R.; Graham, B. S. Respiratory syncytial virus: virology, reverse genetics, and pathogenesis of disease. *Curr. Top Microbiol Immunol* **2013**, *372*, 3−38.
(18) Noton, S. L.; Deflubé, L. R.; Tremaglio, C. Z.; Fearns, R. The Respiratory Syncytial Virus Polymerase Has Multiple RNA Synthesis Activities at the Promoter. *PLOS Pathogens* **2012**, *8* (10), No. e1002980.
(19) Khattar, S. K.; Yunus, A. S.; Samal, S. K. Mapping the domains on the phosphoprotein of bovine respiratory syncytial virus required for N−P and P−L interactions using a minigenome system. *Journal of General Virology* **2001**, *82* (4), 775−779.
(20) Gilman, M. S. A.; Liu, C.; Fung, A.; Behera, I.; Jordan, P.; Rigaux, P.; Ysebaert, N.; Tcherniuk, S.; Sourimant, J.; Eléouët, J.-F.; et al. Structure of the Respiratory Syncytial Virus Polymerase Complex. *Cell* **2019**, *179* (1), 193−204.
(21) Elawar, F.; Oraby, A. K.; Kieser, Q.; Jensen, L. D.; Culp, T.; West, F. G.; Marchant, D. J. Pharmacological targets and emerging treatments for respiratory syncytial virus bronchiolitis. *Pharmacol. Ther.* **2021**, *220*, No. 107712.
(22) Atienza, B. J. P.; Jensen, L. D.; Noton, S. L.; Ansalem, A. K. V.; Hobman, T.; Fearns, R.; Marchant, D. J.; West, F. G. Dual Catalytic Synthesis of Antiviral Compounds Based on Metallocarbene−Azide Cascade Chemistry. *J. Org. Chem.* **2018**, *83* (13), 6829−6842.
(23) Schrödinger, L.; DeLano, W. & 2020, *PyMOL*, http://www.pymol.org/pymol.
(24) Sutto-Ortiz, P.; Tcherniuk, S.; Ysebaert, N.; Abeywickrema, P.; Noël, M.; Decombe, A.; Debart, F.; Vasseur, J.-J.; Canard, B.; Roymans, D.; et al. The methyltransferase domain of the Respiratory Syncytial Virus L protein catalyzes cap N7 and 2'-O-methylation. *PLOS Pathogens* **2021**, *17* (5), No. e1009562.
(25) Le Guilloux, V.; Schmidtke, P.; Tuffery, P. Fpocket: An open source platform for ligand pocket detection. *BMC Bioinf.* **2009**, *10* (1), 168.
(26) Halgren, T. New Method for Fast and Accurate Binding-site Identification and Analysis. *Chem. Biol. Drug Des.* **2007**, *69* (2), 146−148.
(27) Halgren, T. A. Identifying and Characterizing Binding Sites and Assessing Druggability. *J. Chem. Inf. Model.* **2009**, *49* (2), 377−389.
(28) Krivák, R.; Hoksza, D. Improving protein-ligand binding site prediction accuracy by classification of inner pocket points using local features. *J. Cheminf.* **2015**, *7* (1), 12.
(29) Lu, X.; McDonald, S. M.; Tortorici, M. A.; Tao, Y. J.; Vasquez-Del Carpio, R.; Nibert, M. L.; Patton, J. T.; Harrison, S. C. Mechanism for coordinated RNA packaging and genome replication by rotavirus polymerase VP1. *Structure* **2008**, *16* (11), 1678−1688.
(30) Cao, D.; Gao, Y.; Chen, Z.; Gooneratne, I.; Roesler, C.; Mera, C.; D'Cunha, P.; Antonova, A.; Katta, D.; Romanelli, S.; et al. Structures of the promoter-bound respiratory syncytial virus polymerase. *Nature* **2024**, *625* (7995), 611−617.
(31) De Vivo, M.; Masetti, M.; Bottegoni, G.; Cavalli, A. Role of Molecular Dynamics and Related Methods in Drug Discovery. *J. Med. Chem.* **2016**, *59* (9), 4035−4061.
(32) Jacobson, M. P.; Pincus, D. L.; Rapp, C. S.; Day, T. J. F.; Honig, B.; Shaw, D. E.; Friesner, R. A. A hierarchical approach to all-atom protein loop prediction. *Proteins: Struct., Funct., Bioinf.* **2004**, *55* (2), 351−367.
(33) Schmidtke, P.; Bidon-Chanal, A.; Luque, F. J.; Barril, X. MDpocket: open-source cavity detection and characterization on molecular dynamics trajectories. *Bioinformatics* **2011**, *27* (23), 3276−3285.
(34) Cao, D.; Gao, Y.; Roesler, C.; Rice, S.; D'Cunha, P.; Zhuang, L.; Slack, J.; Domke, M.; Antonova, A.; Romanelli, S.; et al. Cryo-EM structure of the respiratory syncytial virus RNA polymerase. *Nat. Commun.* **2020**, *11* (1), 368.
(35) Kleiner, V. A.; Fischmann, T. O.; Howe, J. A.; Beshore, D. C.; Eddins, M. J.; Hou, Y.; Mayhood, T.; Klein, D.; Nahas, D. D.; Lucas, B. J.; et al. Conserved allosteric inhibitory site on the respiratory syncytial virus and human metapneumovirus RNA-dependent RNA polymerases. *Commun. Biol.* **2023**, *6* (1), 649.
(36) Tiong-Yip, C. L.; Aschenbrenner, L.; Johnson, K. D.; McLaughlin, R. E.; Fan, J.; Challa, S.; Xiong, H.; Yu, Q. Characterization of a respiratory syncytial virus L protein inhibitor. *Antimicrob. Agents Chemother.* **2014**, *58* (7), 3867−3873.
(37) Friesner, R. A.; Murphy, R. B.; Repasky, M. P.; Frye, L. L.; Greenwood, J. R.; Halgren, T. A.; Sanschagrin, P. C.; Mainz, D. T. Extra Precision Glide: Docking and Scoring Incorporating a Model of Hydrophobic Enclosure for Protein−Ligand Complexes. *J. Med. Chem.* **2006**, *49* (21), 6177−6196.
(38) Wang, E.; Liu, H.; Wang, J.; Weng, G.; Sun, H.; Wang, Z.; Kang, Y.; Hou, T. Development and Evaluation of MM/GBSA Based on a Variable Dielectric GB Model for Predicting Protein−Ligand Binding Affinities. *J. Chem. Inf. Model.* **2020**, *60* (11), 5353−5365.
(39) Chen, J.; Wang, J.; Zhang, Q.; Chen, K.; Zhu, W. Probing Origin of Binding Difference of inhibitors to MDM2 and MDMX by Polarizable Molecular Dynamics Simulation and QM/MM-GBSA Calculation. *Sci. Rep.* **2015**, *5* (1), 17421.
(40) Weng, Y. L.; Naik, S. R.; Dingelstad, N.; Lugo, M. R.; Kalyaanamoorthy, S.; Ganesan, A. Molecular dynamics and in silico mutagenesis on the reversible inhibitor-bound SARS-CoV-2 main protease complexes reveal the role of lateral pocket in enhancing the ligand affinity. *Sci. Rep.* **2021**, *11* (1), 7429.
(41) Misaki, T.; Nagase, R.; Matsumoto, K.; Tanabe, Y. Ti-Crossed-Claisen Condensation between Carboxylic Esters and Acid Chlorides or Acids: A Highly Selective and General Method for the Preparation of Various β-Keto Esters. *J. Am. Chem. Soc.* **2005**, *127* (9), 2854−2855.
(42) Jiang, X.; Hu, F. One-Pot Highly Regioselective Synthesis of Indole-Fused Pyridazino[4,5-b][1,4]benzoxazepin-4(3H)-ones by a Smiles Rearrangement. *Synlett* **2018**, *29* (09), 1207−1210.
(43) Bott, T. M.; Atienza, B. J.; West, F. G. Azide trapping of metallocarbenes: generation of reactive C-acylimines and domino trapping with nucleophiles. *RSC Adv.* **2014**, *4* (60), 31955−31959.
(44) Jacobson, M. P.; Friesner, R. A.; Xiang, Z.; Honig, B. On the Role of the Crystal Environment in Determining Protein Side-chain Conformations. *J. Mol. Biol.* **2002**, *320* (3), 597−608.
(45) Maier, J. A.; Martinez, C.; Kasavajhala, K.; Wickstrom, L.; Hauser, K. E.; Simmerling, C. ff14SB: Improving the Accuracy of Protein Side Chain and Backbone Parameters from ff99SB. *J. Chem. Theory Comput.* **2015**, *11* (8), 3696−3713.
(46) Mark, P.; Nilsson, L. Structure and Dynamics of the TIP3P, SPC, and SPC/E Water Models at 298 K. *J. Phys. Chem. A* **2001**, *105* (43), 9954−9960.
(47) Vilar, S.; Cozza, G.; Moro, S. Medicinal chemistry and the molecular operating environment (MOE): application of QSAR and molecular docking to drug discovery. *Curr. Top Med. Chem.* **2008**, *8* (18), 1555−1572.
(48) Shelley, J. C.; Cholleti, A.; Frye, L. L.; Greenwood, J. R.; Timlin, M. R.; Uchimaya, M. Epik: a software program for pKaprediction and protonation state generation for drug-like molecules. *J. Comput. Aided Mol. Des.* **2007**, *21* (12), 681−691.
(49) Roos, K.; Wu, C.; Damm, W.; Reboul, M.; Stevenson, J. M.; Lu, C.; Dahlgren, M. K.; Mondal, S.; Chen, W.; Wang, L.; et al. OPLS3e: Extending Force Field Coverage for Drug-Like Small Molecules. *J. Chem. Theory Comput.* **2019**, *15* (3), 1863−1874.

https://doi.org/10.1021/acsomega.4c01207
ACS Omega 2024, 9, 22213−22229

(50) Wang, J.; Wang, W.; Kollman, P. A.; Case, D. A. Automatic atom type and bond type perception in molecular mechanical calculations. *J. Mol. Graph Model* **2006**, *25* (2), 247−260.
(51) Wang, J.; Wolf, R. M.; Caldwell, J. W.; Kollman, P. A.; Case, D. A. Development and testing of a general amber force field. *J. Comput. Chem.* **2004**, *25* (9), 1157−1174.
(52) Jakalian, A.; Jack, D. B.; Bayly, C. I. Fast, efficient generation of high-quality atomic charges. AM1-BCC model: II. Parameterization and validation. *J. Comput. Chem.* **2002**, *23* (16), 1623−1641.
(53) Case, D. A.; Cheatham, T. E., 3rd; Darden, T.; Gohlke, H.; Luo, R.; Merz, K. M., Jr.; Onufriev, A.; Simmerling, C.; Wang, B.; Woods, R. J. The Amber biomolecular simulation programs. *J. Comput. Chem.* **2005**, *26* (16), 1668−1688.
(54) Davidchack, R. L.; Handel, R.; Tretyakov, M. V. Langevin thermostat for rigid body dynamics. *J. Chem. Phys.* **2009**, *130* (23), 234101.
(55) Roe, D. R.; Cheatham, T. E. PTRAJ and CPPTRAJ: Software for Processing and Analysis of Molecular Dynamics Trajectory Data. *J. Chem. Theory Comput.* **2013**, *9* (7), 3084−3095.
(56) Miller, B. R.; McGee, T. D.; Swails, J. M.; Homeyer, N.; Gohlke, H.; Roitberg, A. E. MMPBSA.py: An Efficient Program for End-State Free Energy Calculations. *J. Chem. Theory Comput.* **2012**, *8* (9), 3314−3321.
(57) Elawar, F.; Griffiths, C. D.; Zhu, D.; Bilawchuk, L. M.; Jensen, L. D.; Forss, L.; Tang, J.; Hazes, B.; Drews, S. J.; Marchant, D. J. A Virological and Phylogenetic Analysis of the Emergence of New Clades of Respiratory Syncytial Virus. *Sci. Rep.* **2017**, *7* (1), 12232.

https://doi.org/10.1021/acsomega.4c01207
ACS Omega 2024, 9, 22213−22229